Section 1:
Physics and Detector Performance Metrics

GlueX-doc-9

GlueX/Hall D Conceptual Design Report

1 Physics and Detector Performance Metrics

We start this report on GlueX detector by discussing the physics goals of the GlueX project – mapping the spectrum of gluonic excitations starting with exotic hybrid mesons. We show that the search for exotic mesons depends critically on detecting and measuring the four-momenta of charged particles and photons resulting from the decays of photoproduced mesons. As will be discussed in this report, the majority of the final states that will be studied in GlueX involve a combination of both charged particles and photons. As such, in discussing the performance of the detector, it makes little sense to try and separate these issues.

This report includes information on the electromagnetic calorimetry needed to detect and measure those photons, the tracking chambers that are used to reconstruct the charged particles in GlueX . In addition, a time-of-flight wall is used in conjunction with measurements for other detectors to carry out some particle identification in GlueX. It is the physics goals that determine the performance metrics of the detectors. This includes the granularity, energy, position and timing resolution, and energy thresholds of the calorimeter. It also includes the position resolution of the drift chambers in conjunction with the charged particle tracking which is used to take advantage of timing measurements in both the barrel calorimeter and the time-of-flight wall. Information from the calorimetry will also be used for separating protons from pions and also to provide some information on recoil neutrons. In the central region of the detector, dE/dx measurements in central drift chamber (CDC) will be used to identify π, K and p for low momentum (under $450\,MeV/c$) which are likely to only be seen in the tracking chambers.

The GlueX detector consists of a cylindrical drift chamber (CDC) in the upstream half of a $\sim 4\,m$ long, $2.25\,T$ solenoidal magnet followed by four packages of planar drift chambers (FDC) in the down-stream half of the magnet. A barrel calorimeter (BCAL) surrounds the target and tracking chambers inside the magnet and a down-stream planar calorimeter (FCAL) provides coverage for photons exiting the down-stream hole of the magnet. A time-of-flight wall sits directly in front of the FCAL and space has been left between the end of the magnet and the time-of-flight to accommodate a future particle identification system (probably a ring imaging Chernkov counter).

The requirements on acceptance and on energy, position and timing resolution are driven by the need to identify exclusive reactions in order to perform the amplitude analyses that will extract meson J^{PC} quantum numbers and on the need to be sensitive to a variety of meson decay modes. Generally speaking, good amplitude analysis needs a large and uniform acceptance detector with good resolution for cleanly separating final state, which reduces background leakage into the reactions of interest.

The GlueX does have nearly 4π acceptance for both charged particles and photons. However, that acceptance is not completely uniform in all variables. As with any amplitude analysis, this means that the detector simulation package will need to be able to accurately reproduce the overall detector acceptance. Areas of reduced acceptance include very low momentum charged particles (protons under $300\,MeV/c$ and πs under $150\,MeV/c$, low energy photons, and photons going into the overlap region of the two calorimeters. Substantial work has gone into identifying these problematic regions and minimizing them by design optimization in the detector.

1.1 Physics motivation: the search for exotic mesons

1.1.1 QCD and light meson spectroscopy

The observation, nearly four decades ago, that mesons are grouped in nonets, each characterized by unique values of J^{PC} – spin (J), parity (P) and charge conjugation (C) quantum numbers – led to the development of the quark model. Within this picture, mesons are bound states of a quark (q) and antiquark ($\bar{q}$). The three light-quark flavors (*up*, *down* and *strange*) suffice to explain the spectroscopy of most – but not all – of the lighter-mass mesons (below 3 GeV/c^2) that do not explicitly carry heavy flavors (charm or beauty). Early observations yielded only those J^{PC} quantum numbers consistent with a fermion-antifermion bound state. The J^{PC} quantum numbers of a $q\bar{q}$ system with total quark spin, $\vec{S}$, and relative angular momentum, $\vec{L}$, are determined as follows: $\vec{J} = \vec{L} + \vec{S}$, $P = (-1)^{L+1}$ and $C = (-1)^{L+S}$. Thus J^{PC} quantum numbers such as 0^{--}, 0^{+-}, 1^{-+} and 2^{+-} are not allowed and are called *exotic* in this context.

Our understanding of how quarks form mesons has evolved within quantum chromodynamics (QCD) and we now expect a richer spectrum of mesons that takes into account not only the quark degrees of freedom but also the gluonic degrees of freedom. Gluonic mesons with no quarks (*glueballs*) are expected. These are bound states of pure glue and since the quantum numbers of low-lying glueballs (below 4 GeV/c^2) are not exotic, they should manifest themselves as extraneous states that cannot be accommodated within $q\bar{q}$ nonets. But their unambiguous identification is complicated by the fact that they can mix with $q\bar{q}$. Excitations of the gluonic field binding the quarks can also give rise to so-called *hybrid* mesons that can be viewed as bound states of a quark, antiquark and valence gluon ($q\bar{q}g$). An alternative picture of hybrid mesons, one supported by lattice QCD [9], is one in which a gluonic flux tube forms between the quark and antiquark and the excitations of this flux tube lead to so-called *hybrid* mesons. Actually the idea of flux tubes, or strings connecting the quarks, originated in the early 1970's [10] to explain the observed linear dependence of the mass-squared of hadrons on spin (Regge trajectories). Conventional $q\bar{q}$ mesons arise when the flux tube is in its ground state. Hybrid mesons arise when the flux tube is excited and some hybrid mesons can have a unique signature, exotic J^{PC}, and the spectroscopy of these exotic hybrid mesons is simplified because they do not mix with conventional $q\bar{q}$ states.

The level splitting between the ground state flux tube and the first excited transverse modes is π/r, where r is the separation between the quarks, so the hybrid spectrum should lie about 1 GeV/c^2 above the ground state spectrum. While the flux-tube model [11] has all hybrid nonets degenerate in mass, from lattice gauge calculations [12], one expects the lightest $J^{PC} = 1^{-+}$ exotic hybrid to have a mass of about 1.9 GeV/c^2. In this discussion the motion of the quarks was ignored, but we know from general principles [11] that an approximation that ignores the impact of the flux tube excitation and quark motion on each other seems to work quite well. It should be noted, also, the in the large-N_c limit of QCD, exotic hybrids are expected to have narrow widths, comparable to $q\bar{q}$ states [13].

In the coming years there will be significant computational resources dedicated to understanding non-perturbative QCD including confinement using lattice techniques. The prediction of the hybrid spectrum, including decays, will be a key part of this program but experimental data will be needed to verify these calculations. The spectroscopy of exotic mesons provides a clean and attractive starting point for the study of gluonic excitations.

The GlueX experiment is designed to collect high quality and high statistics data on the photoproduction of light mesons. As part of the program of identifying exotic hybrid mesons, these data will also be used to understand the conventional meson spectrum including the poorly understood excited vector mesons.

1.1.2 Using linearly polarized photons

There are tantalizing suggestions, mainly from experiments using beams of π mesons, that exotic hybrid mesons exist. The evidence is by no means clear cut, owing in part, to the apparently small production rates for these states in the decay channels examined. It is safe to conclude that the extensive data collected to date with π probes have not uncovered the hybrid meson spectrum. (A recent paper by E. Klempt and A. Zaitsev gives an encyclopedic and critical overview of the current experimental situation with regard to searches for glueballs, hybrids and multiquark mesons[14].) Models, like the flux-tube model, however, indicate the photon is a probe that should be particularly effective in producing exotic hybrids, but data on photoproduction of light mesons are sparse indeed.

The first excited transverse modes of the flux tube are degenerate and correspond to clockwise or counterclockwise rotations of the flux tube about the axis joining the quark and antiquark fixed in space with $J = 1$ [11]. Linear combinations of these two modes are eigenstates of parity and lead to $J^{PC} = 1^{+-}$ and $J^{PC} = 1^{-+}$ for the excited flux tube. When these quantum numbers are combined with those of the $q\bar{q}$ with $\vec{L} = 0$ and $\vec{S} = 1$ (quark spins aligned) three of the six possible J^{PC} have exotic combinations: 0^{+-}, 1^{-+} and 2^{+-}. A photon probe is a virtual $q\bar{q}$ with quark spins aligned. In contrast when the $q\bar{q}$ have $\vec{L} = 0$ and $\vec{S} = 0$ (spins anti-aligned), the resulting quantum numbers of the hybrid meson are not exotic. Pion probes are $q\bar{q}$ with quark spins anti-aligned. If we view one outcome of the scattering process as exciting the flux tube binding the quarks in the probe, the suppression of exotic hybrids in π-induced reactions is not surprising – a spin flip of one of the quarks is required followed by the excitation of the flux tube. In contrast the spins

of the virtual quarks in the photon probe are properly aligned to lead to exotic hybrids. Phenomenological studies quantitatively support this picture predicting that the photoproduction cross-sections for exotic mesons are comparable to those for conventional mesons [15].

Determining the quantum numbers of mesons produced in the GlueX experiment will require an amplitude analysis based on measuring the energy and momentum of their decay products. Linear polarization of the incident photon is required for a precision amplitude analysis to identify exotic quantum numbers, to understand details of the production mechanism of exotic and conventional mesons and to remove backgrounds due to conventional processes. Linear polarization will be achieved using the coherent bremsstrahlung technique.

For the GlueX solenoid-based detector system, given the required mass reach required for mapping the spectrum of exotic hybrid mesons, a photon energy of ≈ 9 GeV is ideal. To achieve the requisite degree of linear polarization for 9 GeV photons using coherent bremsstrahlung requires a minimum electron energy of 12 GeV.

1.1.3 Expected decay modes of exotic hybrid mesons

Table 1.1 lists predicted J^{PC} exotic mesons and their decay modes. According to the flux tube model and verified by lattice QCD [16], the preferred decay modes for exotic hybrids are into $(q\bar{q})_P + (q\bar{q})_S$ mesons such as $b_1 + \pi$ or $f_1 + \pi$. Table 1.2 lists candidate exotic $J^{PC} = 1^{-+}$ state for which evidence has been claimed. The purported exotic states include decay modes into $b_1\pi$ or $f_1\pi$ as well as decay modes into $\eta\pi$ and $\eta'\pi$. The dominant branching fractions for meson states listed among the decay products are summarized in Table 1.3. Clearly, exotic meson spectroscopy requires the ability to detect and measure charged particles as well as π^0 and η mesons.

Some of the preferred or observed exotic hybrid decay modes listed in Tables 1.1 and 1.2 do not necessarily involve π^0 mesons, *e.g.* the $\rho\pi$ or $a_2\pi$ modes – these can have final states that only involve $\pi^\pm$ such as $(\rho\pi)^+ \to \pi^+\pi^+\pi^-$. But if a state decays into such an all charged π system, having the isospin partners available, such as $(\rho\pi)^+ \to \pi^+\pi^0\pi^0$ provides important isospin consistency checks of the amplitude analysis and understanding of the detector acceptance.

Exotic Meson	J^{PC}	I	G	Possible Modes
b_0	0^{+-}	1	+	
h_0	0^{+-}	0	−	$b_1\pi$
π_1	1^{-+}	1	−	$\rho\pi$, $b_1\pi$
η_1	1^{-+}	0	+	$a_2\pi$
b_2	2^{+-}	1	+	$a_2\pi$
h_2	2^{+-}	0	−	$\rho\pi$, $b_1\pi$

Table 1.1: Predicted J^{PC} exotic hybrid mesons and their expected decay modes. See Table 1.3 for decay modes of the b_1 and a_2 mesons.

Exotic Meson Candidate	Decay Mode
$\pi_1(1400)$	$\pi^-\eta$
	$\pi^0\eta$
$\pi_1(1600)$	$\rho^0\pi^-$
	$\eta'\pi^-$
$\pi_1(1600/2000)$	$b_1\pi$
	$f_1\pi$

Table 1.2: Reported $J^{PC} = 1^{-+}$ exotic hybrid mesons and their decay modes. See Table 1.3 for decay modes of the η', b_1 and f_1 mesons. Source: 2006 Review of Particle Physics [17].

Meson Decay Mode	Branching Fraction (%)
$\pi^0 \to 2\gamma$	99
$\eta \to 2\gamma$	39
$\eta \to 3\pi^0$	33
$\eta \to \pi^+\pi^-\pi^0$	23
$\omega \to \pi^+\pi^-\pi^0$	89
$\omega \to \pi^0\gamma$	9
$\eta' \to \pi^+\pi^-\eta$	45
$\eta' \to \pi^0\pi^0\eta$	21
$\eta' \to 2\gamma$	2
$b_1(1235) \to \omega\pi$	dominant
$f_1(1285) \to \pi^0\pi^0\pi^+\pi^-$	22
$f_1(1285) \to \eta\pi\pi$	52
$a_2(1320) \to 3\pi$	70
$a_2(1320) \to \eta\pi$	15

Table 1.3: Neutral or charged + neutral decay modes of several well established mesons. Source: 2006 Review of Particle Physics [17].

1.2 Detector overview

To achieve the primary physics goal of GlueX, *i.e.* mapping out the spectrum of gluonic excitations, it is essential to detect charged partciles and photons with good acceptance and to measure their momentum, energies and positions with sufficient resolution. Charged particles include $\pi^{\pm}$, $K^{\pm}$ and protons, while the photons of particular interest are those resulting from $\pi^0 \to \gamma\gamma$ and $\eta \to \gamma\gamma$ decays. The GlueX detector, as shown in Figure 1.1, includes two tracking systems and two electromagnetic calorimeters to detect and measure these particles.

The GlueX detector is a solenoidal detector that is ideally suited for a fixed target photoproduction experiment. The solenoidal magnetic field traps low energy electromagnetic backgrounds (e^+e^- pairs), generated in the target, inside a small diameter beam hole that runs through the detector. The superconducting solenoid magnet produces a 2 T field. The photon beam is incident on a 30-cm LH_2 target that is surrounded by a cylindrical tracking chamber and a cylindrical electromagnetic calorimeter. Downstream of the target are circular planar tracking chambers and a circular planar electromagnetic calorimeter.

1.3 Information from existing photoproduction data

There is little data on meson photoproduction in the GlueX energy regime ($E_\gamma \approx 7 - 9$ GeV). Almost all of what is known comes from bubble chamber measurements at SLAC [18, 19, 20, 21, 22, 23]. These experiments were among the first exploratory studies of the photoproduction of meson and baryon resonances at these energies, and although they suffer from low-statistics, they have good acceptance, except for events with multiple neutrals. Exclusive reactions leading to final states with charged particles and a single neutron or π^0 can be identified by kinematic fitting. Table 1.4 summarizes the photoproduction cross sections for various charged particle topologies, with and without neutrals, at $E_\gamma = 9.3$ GeV [18]. Final states with single or multi-neutral particles (π^0, η or n) account for about 82% of the total cross section. About 13% of the total cross section is due to final states with charged particles and a single π^0. So for about 70% of the total photoproduction cross section, from $E_\gamma \approx 7$ to ≈ 12 GeV, we have essentially no information. Extrapolating from what is known from the final states that have been identified and studied, the bulk of the unknown processes are expected to involve final states with combinations of π^0 and η mesons. The discovery potential of GlueX rests on being able to detect π^0 and η mesons in addition to the charged particles.

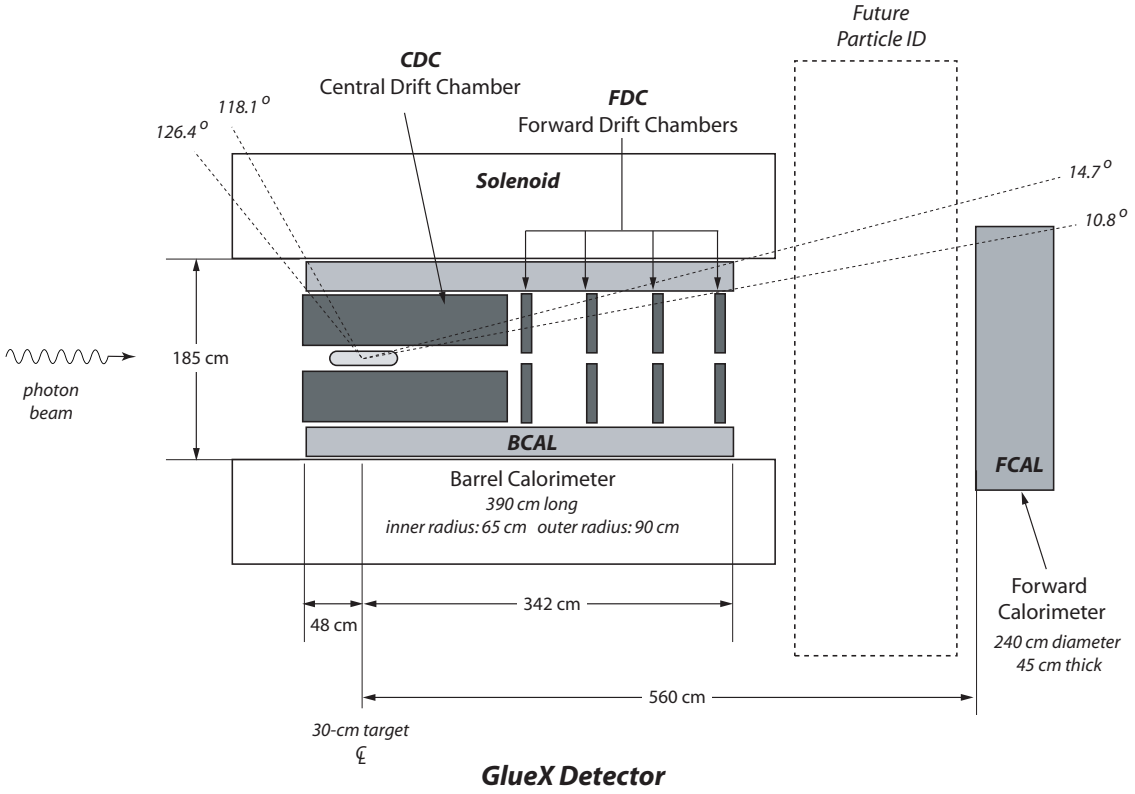

Figure 1.1: Schematic of the GlueX Detector. The superconducting solenoid magnet produces a 2 T field. The photon beam is incident on a 30-cm LH_2 target that is surrounded by a cylindrical tracking chamber (CDC) and a cylindrical electromagnetic calorimeter (BCAL). Downstream of the target are circular planar tracking chambers (FDC) and a circular planar electromagnetic calorimeter (FCAL). The dimensions of BCAL and FCAL are shown. The detector has cylindrical symmetry about the beam direction. The dashed lines at angles (with respect to the beam direction) 10.8° through 126.4° will be referenced in the text.

Baryon resonance decays: Photoproduction of meson resonances in the GlueX energy regime typically result in the meson being produced at small absolute values of the momentum transfer squared $|t|$ between incoming photon and outgoing meson – or equivalently between target proton and recoil nucleon or baryon resonance. The produced meson, as well as its decay products (depending on the particle multiplicity and relative mother-daughter masses), move in the forward direction whereas the recoil baryon moves at large angles $\gtrsim 45°$ with respect to the beam direction. If the recoil baryon is a baryon resonance, such as a Δ or N^*, decays involving π^0 are possible. It will be important to identify the soft, wide-angle π^0 mesons from such decays since the amplitude analysis depends on starting with a known exclusive reaction.

1.3.1 Studies using PYTHIA

As noted above, much is unknown about photoproduction at GlueX energies leading to multi-neutral final states. To estimate photon yields we used the Monte Carlo program PYTHIA [24] that was written to generate high energy physics events produced in a wide variety of initial states, including fixed target photoproduction. The program is based on a combination of analytical results and QCD-based models of particle interactions. PYTHIA was designed to allow for tuning parameters to suit the particular situation – for example, photoproduction at 9 GeV. The output of the simulations were compared [25] to published data, in particular, reference [18]. Comparison of cross section estimates for charged particle topologies and

Topology	σ (μb)	% of σ with neutrals
1-prong	8.5 ± 1.1	100
3-prong	64.1 ± 1.5	76 ± 3
5-prong	34.2 ± 0.9	86 ± 4
7-prong	6.8 ± 0.3	86 ± 6
9-prong	0.61 ± 0.08	87 ± 21
With visible strange decay	9.8 ± 0.4	-
Total	124.0 ± 2.5	82 ± 4

Table 1.4: Topological photoproduction cross sections for γp interactions at 9.3 GeV from Reference [18]. Also shown are the percent of the cross section with neutral particles for each topology.

several reactions in the 3-prong and 5-prong, which accounts for 80% of the total cross section, are shown in Tables 1.5 and 1.6. The vector mesons ρ, ω and ϕ appear in the 3-prong sample in the $\pi^+\pi^-p$, $\pi^+\pi^-\pi^0p$ and K^+K^-p final states respectively. The distribution in $|t|$ for PYTHIA events agrees with published data for specific reactions. PYTHIA accounts for Δ resonance production. In the $\pi^+\pi^-K^+K^-p$ state, the $K^*(890)$ is present.

Topology	PYTHIA Estimates (μb)	Data (μb)
1-prong	8.8 ± 0.02	8.5 ± 1.1
3-prong	63.5 ± 0.09	64.1 ± 1.5
5-prong	42.7 ± 0.2	34.2 ± 0.9
7-prong	7.3 ± 0.1	6.8 ± 0.3
9-prong	0.3 ± 0.1	0.61 ± 0.08

Table 1.5: Topological Photoproduction Cross Sections at 9 GeV from PYTHIA and from bubble chamber data [18]. The PYTHIA cross section estimates have been tuned to a total photoproduction cross section of 124 μb. The errors on the PYTHIA estimates are statistical.

1.4 Particle Kinematics in GlueX

In this section, we examine the kinematic coverage of both charged particles and photons in the GLUEX detector.

1.4.1 π^0 and η Kinematics

Here we review how the decay photons from photoproduced meson and baryon resonances populate LAB energy-angle space at GLUEX energies. Please refer to Figure 1.1 that shows a schematic of the GLUEX detector. Note the dotted lines showing angles at 10.8° and 126.4°. Photons whose angles lie within this range will be detected and measured by BCAL. Photons with angles between 1° and 10.8° will be detected and measured by FCAL. Photons whose angles are greater than 126.4° or less than 1° will be undetected.

Photon distributions in energy and angle: We now use this version of PYTHIA tuned to provide reasonable agreement with published data, to provide estimates of the multiplicity of photons in the GLUEX calorimeters along with their energies and angles. Figure 1.2 shows photon information for 1M PYTHIA events. About 78% of the events have at least one photon leading to a 3.2M photon sample. The photon multiplicity is shown in Figure 1.2(a) The correlation of photon energy with angle is shown for all photons in BCAL (Figure 1.2(b)), in FCAL (Figure 1.2(c)) and for photons with angles greater than 126° (Figure 1.2(d)). The percentage of all photons entering FCAL is 27.3%, entering BCAL is 70.5%, with angles greater than 126° is 1.7% and entering the beam hole in FCAL (defined by angles less than 1°) is 0.5%. So BCAL and FCAL

Reaction	PYTHIA Estimates (μb)	Data (μb)
	$\gamma p \to 3$ prongs	
$\gamma p \to p\pi^+\pi^-$	13.6 ± 0.13	14.7 ± 0.6
$\gamma p \to pK^+K^-$	0.41 ± 0.02	0.58 ± 0.05
$\gamma p \to p\bar{p}p$	0.04 ± 0.01	0.09 ± 0.02
$\gamma p \to p\pi^+\pi^-\pi^0$	5.8 ± 0.1	7.5 ± 0.8
$\gamma p \to n2\pi^+\pi^-$	1.4 ± 0.04	3.2 ± 0.7
With multi-neutrals	42.3 ± 0.3	38.0 ± 1.9
	$\gamma p \to 5$ prongs	
$\gamma p \to p2\pi^+2\pi^-$	2.9 ± 0.06	4.1 ± 0.2
$\gamma p \to pK^+K^-\pi^+\pi^-$	0.51 ± 0.03	0.46 ± 0.08
$\gamma p \to p2\pi^+2\pi^-\pi^0$	8.12 ± 0.1	6.7 ± 1.0
$\gamma p \to n3\pi^+2\pi^-$	$0.8 \pm .3$	1.8 ± 1.9
With multi-neutrals	30.4 ± 0.2	21.1 ± 1.7

Table 1.6: Photoproduction reaction cross sections at 9 GeV from PYTHIA and from bubble chamber data [18]. The PYTHIA cross section estimates have been tuned to a total photoproduction cross section of 124 μb. The errors on the PYTHIA estimates are statistical.

together will be illuminated by about 98% of all photons with BCAL having about 2.5 times more photons than FCAL. The implications of not detecting the 1.7% of photons that have angles greater than 126° will be discussed below.

Energy threshold: An important parameter for either calorimeter is the energy threshold. Table 1.7 shows the fraction (in percent) of events with more than one photon in a calorimeter for which the minimum energy in the event is less than the threshold energy. These are percentages obtained by averaging over all topologies (charged and neutral particles). As will be seen below, for some signature reactions in GLUEX involving multiple photons and charged particles, the overall event acceptance will depend critically on the minimum energy at which a photon can be reconstructed.

Energy Threshold E_{thr} (MeV)	BCAL: % with $E_{min} < E_{thr}$	FCAL: % with $E_{min} < E_{thr}$
20	2	0
40	5	0.1
50	8	0.2
100	17	1.9
150	25	4.8

Table 1.7: Fraction (in percent) of events with more than one photon in a calorimeter for which the minimum energy in an event is less than the threshold energy.

BCAL granularity: The plots of Figure 1.3 address the issue of the granularity needed for BCAL. Distributions for (a) photon multiplicity in BCAL for events with one or more photons in BCAL; (b) separation of photons in azimuthal angle for photons in BCAL (multiple entries per event); and (c) minimum azimuthal angle separation in an event are shown. Also shown is the correlation of azimuthal separation (all di-photon combinations in an event) with photon multiplicity. As will be described below (in the BCAL section) the BCAL readout cell size is approximately 2×2 cm^2. The in depth (along the radius) the segmentation is exactly 2 cm and along the azimuth the width varies with depth to correspond to an azimuthal segmentation of 1.875°. This segmentation is for the first 12 cm in depth but it accounts for providing the bulk of information needed for photon reconstruction. Also, as will be discussed below, the segmentation for the

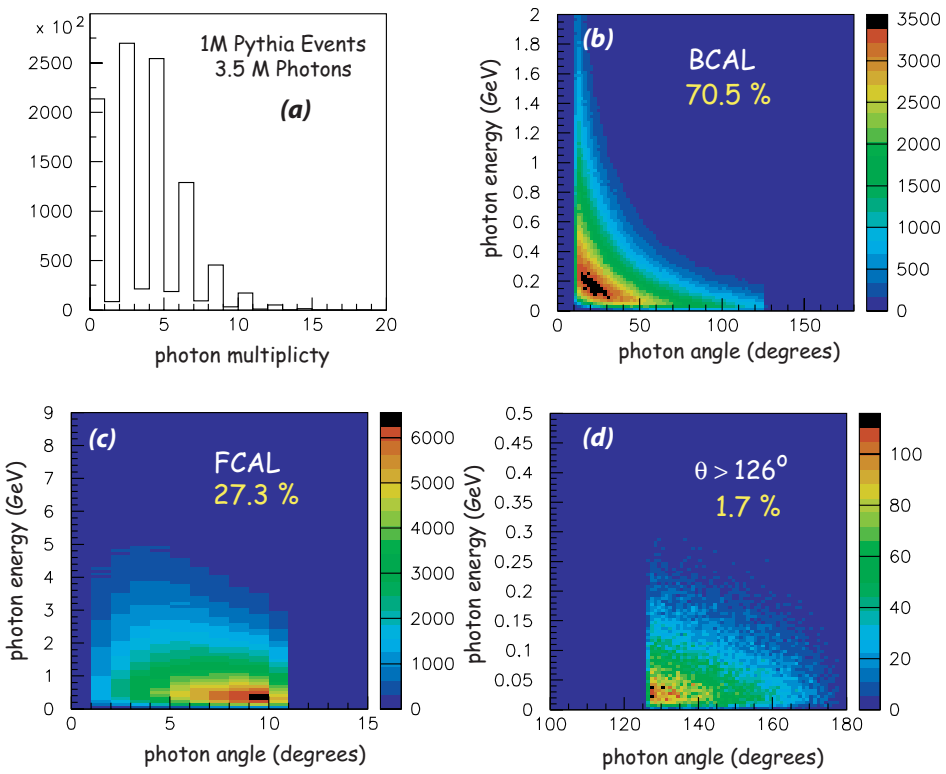

Figure 1.2: (a) Photon multiplicity for 1M PYTHIA events. About 78% of the events have at least one photon leading to a 3.2M photon sample. The correlation of photon energy with angle is shown for photons in (b) BCAL, (c) FCAL and (d) for photons with angles greater than 126°. Note that the plot axes have different scales.

remaining depth has a coarser segmentation. This cell size is a good match to the BCAL Molière radius (3.6 cm). Approximately 6% of events with two or more photons in BCAL have a photon pair with an azimuthal angular separation less than 2°.

FCAL granularity: The plots of Figure 1.4 address the issue of the granularity needed for FCAL. Distributions for (a) photon multiplicity in FCAL for events with one or more photons in FCAL; (b) photon distance from center of FCAL in the plane of FCAL; and (c) photon separation in the plane of FCAL (multiple entries per event) are displayed. Also shown is the (d) (x,y) pattern of photon hits on the plane of FCAL.

The specific design of FCAL will be discussed in more detail below, but for now we note that the design follows the granularity used in E852 [3, 4] and RADPHI [5, 6] based on glass blocks with transverse dimensions of 4×4 cm^3. These dimensions are a good match to the Molière radius (4.3 cm) of the lead glass that will be used in FCAL. These PYTHIA simulations show that the percentage of all events with two or more photons in FCAL, 0.7% of these events have a minimum di-photon separation of 8 cm or less. The maximum energy π^0 (E_π^{max}) expected for GLUEX is 9 GeV for nominal running with polarized photons and 12 GeV for photon running near the electron endpoint energy. This corresponds to a minimum di-photon separation of 16 and 13 cm for the two energies, using $\Delta r = 2m_\pi L_{FCAL}/E_\pi^{max}$ with $L_{FCAL} = 560$ cm (see Figure 1.1).

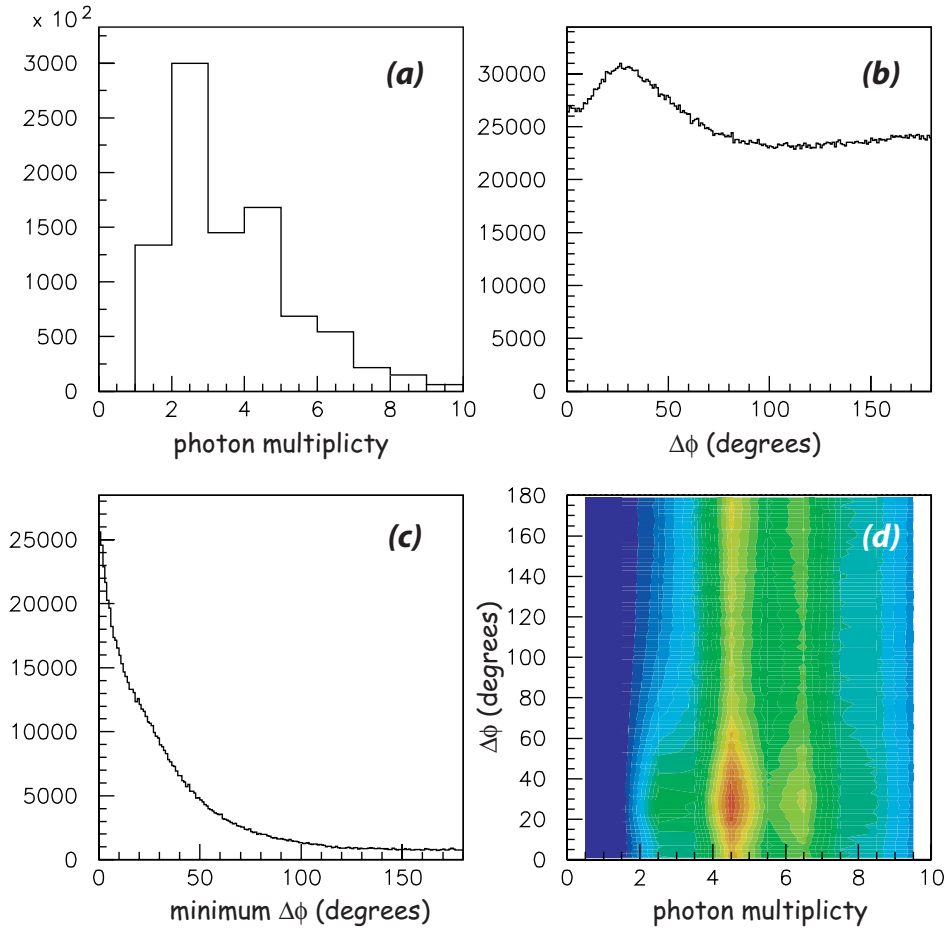

Figure 1.3: Photons in BCAL: distributions in (a) photon multiplicity in BCAL for events with one or more photons in BCAL; (b) separation of photons in azimuthal angle for photons in BCAL (multiple entries per event); (c) minimum azimuthal angle separation in an event; (d) correlation of azimuthal separation (all di-photon combinations in an event) with photon multiplicity.

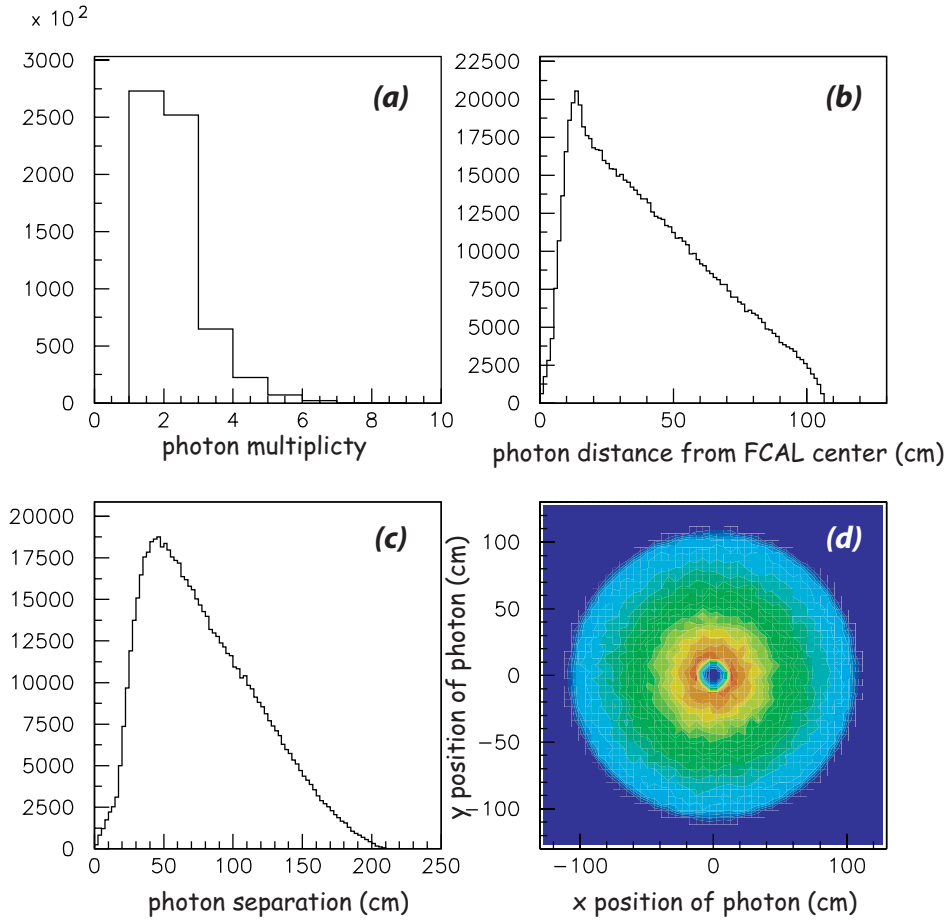

Figure 1.4: Photons in FCAL: distributions in (a) photon multiplicity in FCAL for events with one or more photons in FCAL; (b) photon distance from center of FCAL in the plane of FCAL; (c) photon separation in the plane of FCAL (multiple entries per event); and (d) (x,y) pattern of photon hits on the plane of FCAL.

1.4.2 Charged particles in GlueX

Charged particles ($\pi^{\pm}$, $K^{\pm}$ and p) will be reconstructed using two tracking systems. The CDC around the target and the FDC in the down-stream half of magnet. The CDC [7] is a 24-layer, 1.5m long straw tube chamber while the FDC [8] packages are cathode-plane drift chambers. These are described in detail later documents. Here we only cite that the CDC should achieve a 150 μm resolution normal to the wire. Using stereo layers, a z resolution along the wire of about $\sim$ 1.5mm can be achieved. The FDC will make measurements in the x-y plane (normal to the beam direction) with a resolution of 200 μm. Together, these detectors will track particles from threshold up to nearly 8 GeV/c. The kinematics of the photoproduction reaction tend to give the particles a forward boost with the highest momentum particles traveling at small angles and essentially detected only in the FDC. Particles with larger transverse momentum tend to have lower over all momentum and will be tracked in some combination of the two chambers.

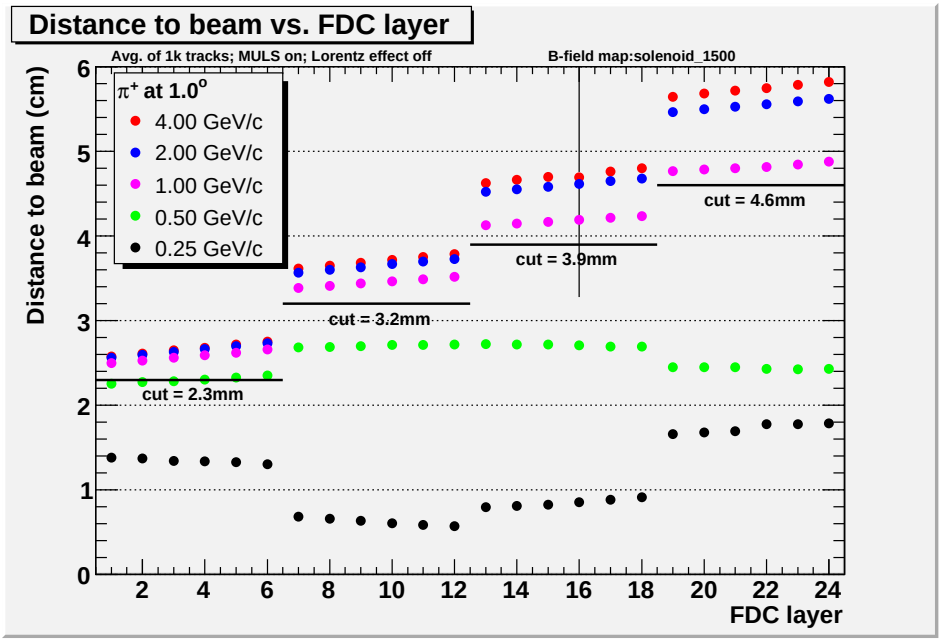

Figure 1.5: The forward hole near the beamline in the FDC is defined by the requirement that 1 GeV/c π^+ with $\theta = 1°$ will be measured in the FDC. The plots shows the maximum size of the hole around the beamline in each FDC package for various values of the π^+ momentum at 1°. The odd structure for 0.5 GeV/c and 0.25 GeV/c particles occurs due to spiraling of the tracks in the solenoidal field.

Semi-quantitatively, particles going more forward than about 1° in the lab will go down the beamline and not be seen by any tracking detector. Outside of this to about 6°, particles will be seen only in the FDC. From 6° out to 30°, particles can be seen by both the CDC and the FDC. Realistically, for both the CDC and the FDC to be used in reconstruction, the particles are in the range of about 8° to 24°. From 30° to about 150°, particles can be reconstructed in the CDC, and hits will be seen in the CDC back to 168°, but resolution is likely to be poor due to there being fewer than 10 hits on a track.

The Forward Hole: More precisely, the forward hole in the GlueX acceptance has been defined by background rates in the FDC detectors. These background rates limit the size of the hole to about 1° in polar angle (θ). To make the hole uniform in all four FDC packages, the hole is defined by tracking 1GeV/c π^+ through the detector and measuring the distance from the beam line in each of the four FDC packages. The result of this is shown in Figure 1.5. In particular, the first FDC package has a hole that is 2.3mm in radius and the fourth package has a hole that is 4.6mm in radius.

As can be seen in Figure 1.5, the angular size of the forward hole becomes somewhat smaller as momentum is increased above 1GeV/c and is larger for lower momenta. In particular, the curves which correspond to 0.25GeV/c and 0.5GeV/c show what appears to be an odd structure in the Figure. In fact, it is just the particles spiraling in the magnetic field as they move through the detector. Particles with 0.25GeV/c momentum are on the innermost part of a spiralling loop in FDC packages two and three. Because of spiraling of these low momentum particles, it does not make a great deal of sense to use them in defining the size of the forward hole.

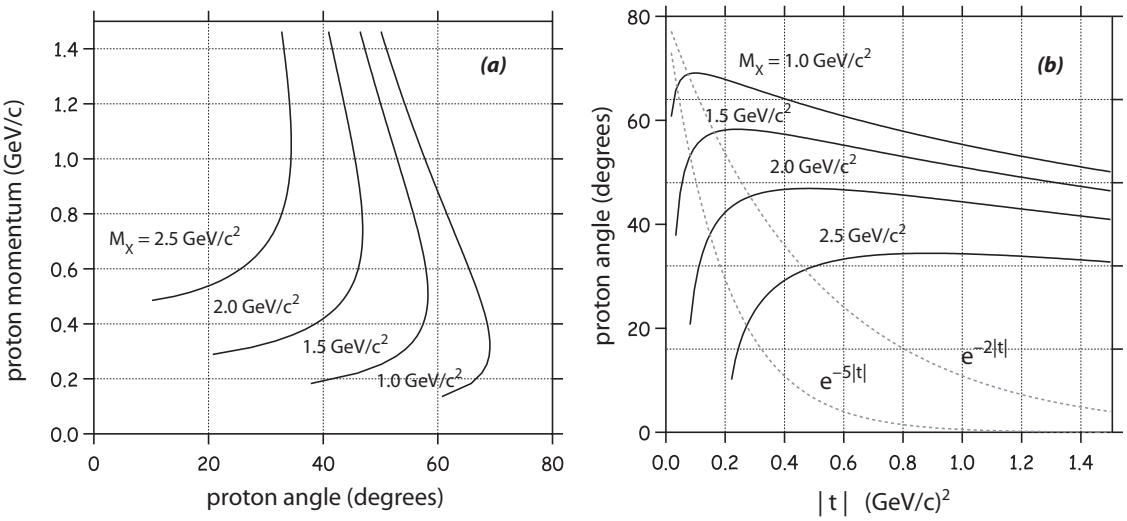

Figure 1.6: (a) Recoil proton LAB momentum as a function of proton LAB angle, measured with respect to the beam direction, for $\mid t \mid_{min} < 1.5\,(GeV/c)^2$ for the reaction $\gamma p \rightarrow Xp$ for $M_X = 1.0, 1.5, 2.0$ and $2.5\,GeV/c^2$. (b) Recoil proton LAB angle, measured with respect to the beam direction as a function of $\mid t \mid$ for the reaction $\gamma p \rightarrow Xp$ for $M_X = 1.0, 1.5, 2.0$ and $2.5\,GeV/c^2$. Also shown are typical t distributions for $e^{-2|t|}$ and $e^{-5|t|}$ (light dotted curves).

Reactions of Interest for Hybrid Mesons: In order to understand how particles of various momentum populate the tracking elements, we need to consider some typical reactions which are part of the GlueX physics program. The first of these is the generic reaction $\gamma p \rightarrow pX$, where X represents a mesonic system whose mass can go up to around $2.5\,GeV/c^2$. Such a reaction is expected to be produced in a t-channel process where the cross section has an exponential dependence on the magnitude of t, $e^{-\alpha|t|}$, with the slope, α varying from 2 to 5. Such a reaction defines the proton kinematics in the GlueX detector. Figure 1.6 shows the lab momentum and angles for protons produced in the reaction $\gamma p \rightarrow pX$ with X varying in mass from 1.0 up to $2.5\,GeV/c^2$. Virtually all of these protons are seen in the forward half of the CDC, with many of them also seen in the FDC packages. For $m_X = 2.5\,GeV/c^2$, the most forward protons have a total momentum of about $0.4\,GeV/c$ with this momentum becoming smaller as the mass of X gets smaller.

A signature reaction for GlueX is $\gamma p \rightarrow n\pi^+\pi^+\pi^-$, where the 3π system has a mass in the range of 1.5 to $2.5\,GeV/c^2$. The distributions of charged pions from this reaction shown in Figure 1.7. About 50 % of these pions are only seen in the FDC. Most of the remainder are seen in both the CDC and FDC with a tail of particles below about $1.5\,GeV/c$ seen only in the CDC. Other important reactions have larger numbers of pions, (4, 5, 6, $\cdots$). As the final state multiplicity becomes larger, the average particle momentum gets smaller, and slower particles are seen at larger angles in the CDC. For the reactions of interest for amplitude analysis in GlueX, the detector acceptance very good for all of these reactions.

The hybrid strangonium states are expected to decay predominantly through several final states which eventually populate the reaction $\gamma p \rightarrow pK^+K^-\pi\pi$. Within this final state, the following reactions are

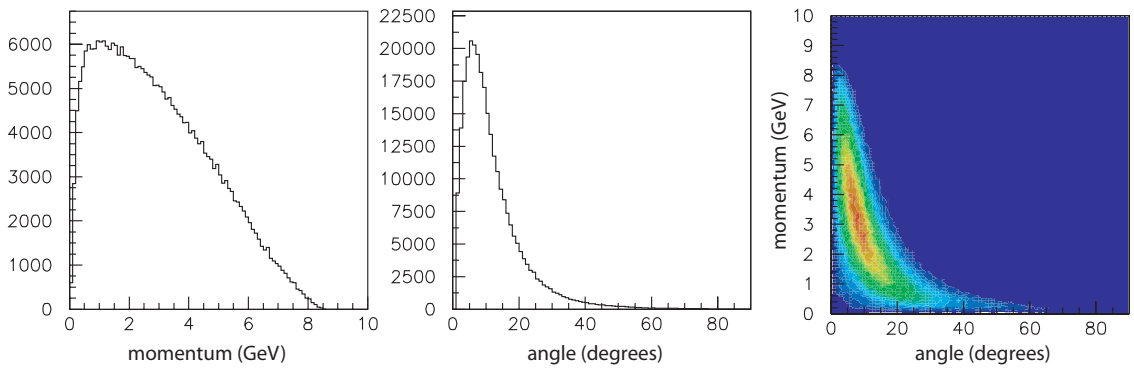

Figure 1.7: The momentum and angle spectra of charged pions and their correlation from the reaction $\gamma p \rightarrow \pi^+\pi^+\pi^- n$ for 8.5 to 9.0 GeV photons.

predicted by decay models to be the dominant decay modes.

$$\begin{aligned}
\gamma p &\rightarrow K_1^{\pm}(1410)K^{\mp} \\
\gamma p &\rightarrow K_1^{\pm}(1270)K^{\mp} \\
\gamma p &\rightarrow K^*(892)\bar{K}^*(892) \\
\gamma p &\rightarrow \phi(1020)f_0(980)
\end{aligned}$$

Assuming t-channel production, the distribution of kaon momentum versus angle are shown in Figure 1.8 for the four reactions above, where one assume a t slope of $\alpha = 5$ and a hybrid mass in the range of 2 to 2.5 GeV/c^2—in line with all current hybrid predictions. These kaons tend to populate both the FDC and the forward part of the CDC and have momenta from several hundred MeV/c up to nearly 6 GeV/c, with the highest momentum tending to be in the very forward direction. In terms of reconstructing the charged particles, this is a very good match to the GlueX tracking systems.

All of the reactions examined above tend to populate the GlueX tracking system with angles well forward of 90° in the lab. This is true for t-channel processes where a neutron or proton is connected to the lower vertex—the expected hybrid production mechanism. However, a competing reaction ($\gamma p \rightarrow \Delta X$) can generate both charged and neutral pions at more backwards angles. In this case, the pion from the decay of the Δ can by sent into the backwards direction. For charged particles, the acceptance of GlueX is still very good for these relatively slow pions.

Low Momentum Cutoffs: Monte Carlo studies have been carried out to quantify the the low-momentum thresholds for charged particles in GlueX. These cutoffs are dominated by energy loss in material before reaching the tracking volumes as well as bending in the strong magnetic field. If we consider particles that are nominally seen by the CDC, the cutoff as a function of polar angle from 15° to 90° in the lab and momentum is shown in Figure 1.9. Pions with momenta smaller than about 0.15 GeV/c cannot be reconstructed in GlueX . For kaons, the cutoff is similar to pions at large angles, but rises to about 0.22GeV/c for forward going Ks. Protons have a more difficult time with the cut off falling from about 0.33GeV/c in forward directions down to about 0.25GeV/c at 90° in the lab. In terms of overall reconstruction, the missing proton produces the largest hole in the GlueX acceptant. Combining this cut off with the information in Figure 1.6, we see that for mesons systems (X) with masses below about 2 GeV/c^2, the low-t production will tend to produce a proton that will not be easily detected in GlueX . These protons will have to be reconstructed using kinematic fitting and missing mass techniques.

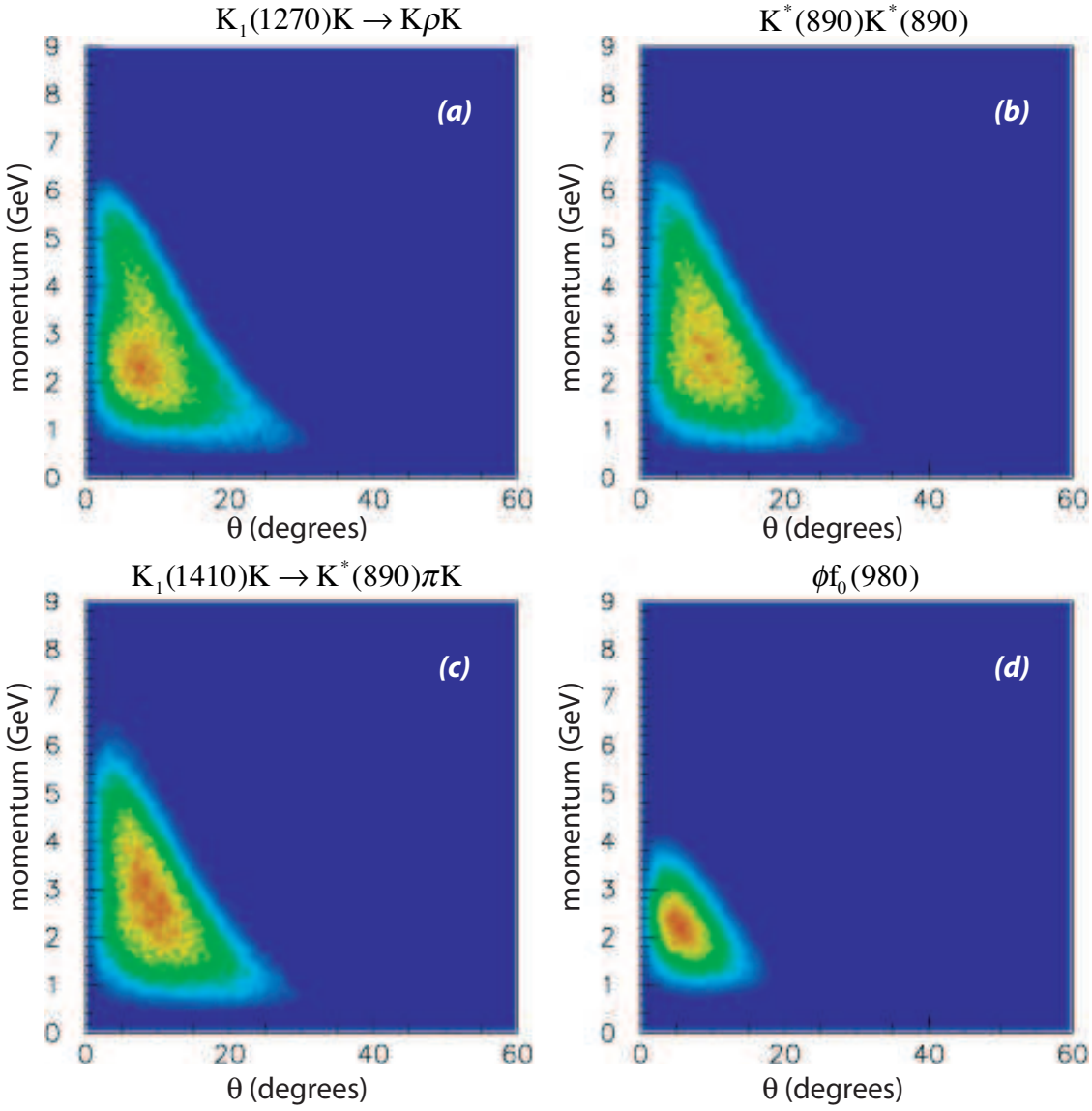

Figure 1.8: The momentum versus angle (in the lab) for $K^{\pm}$ in the reaction $\gamma p \to pK^+K^-\pi\pi$ for various intermediate states. (a) $K_1^{\pm}(1270)K^{\mp}p$; (b) $K^*(890)\bar{K}^*(890)$; (c) $K_1^{\pm}(1410)K^{\mp}p$; and (d) $\phi(1020)f_0(980)$.

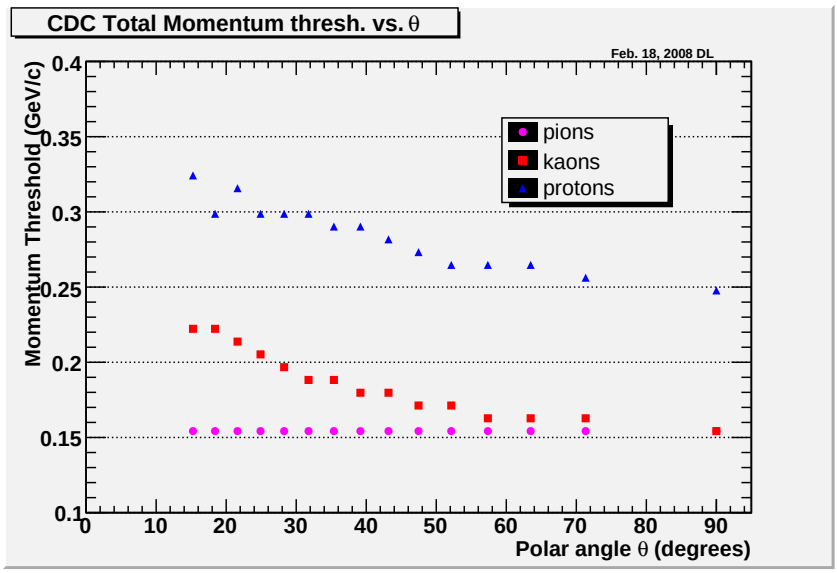

Figure 1.9: Momentum threshold for reconstructing charged particles in the CDC.

1.5 Photon coverage at large angles

As noted in Figure 1.1, there is no photon detection for photons with angles $> 126^\circ$ and from Table 1.9 we see that the percentage of all photons for PYTHIA events and for $\eta\pi^0$ events that populate this angular is small. The class of photoproduction reactions that populate this angular region with photon are reactions resulting in the production of a forward meson (X) and a recoil excited baryon decaying into $\pi^0 p$ or $\pi^0 n$. Since the application of the amplitude analysis depends on identification of exclusive final states, it will be important to identify such reactions by explicitly measuring the decay products of the baryon resonance or to veto events offline that have a extraneous π^0 or photons too low in energy to be identified kinematically given the limitations on resolution in missing mass.

To understand the effect of the presence of baryon resonances we generated $\gamma p \to X\Delta$ events where X is a resonance of mass uniformly distributed between 1.0 and 2.0 GeV/c^2 and produced with a distribution in momentum transfer squared (t) given by $e^{-5\cdot|t|}$. The Δ mass and width are 1.236 and 0.15 GeV/c^2 respectively and the decay mode is $\pi^0 N$. The kinematics of the recoil baryon is determined by the value of $|t|$ and is independent of M_X expect for the dependence of $|t|_{min}$ on M_X. The percent of all photons generated that populate various angular regions is summarized in Table 1.9. The percentage of photons with angles $> 126^\circ$ is relatively large but these events can be tagged for elimination by using information from FCAL and BCAL, but primarily the latter. For the sample generated, 80% of the events have both photons from the π^0 (the Δ decay product) in BCAL and 85% have both photons in either FCAL or BCAL or shared between the two. Only 0.3% of the events have no photons in either FCAL or BCAL so effectively more than 99% of the baryon resonance events can either be measured or tagged.

Extending the upstream end of BCAL by 30 cm would increase the backward angle coverage to 140° and would recover about 50% of the backwards-going photons that are now missed. Extending to 140° would recover 70% of the photons missed with the current configuration but would require adding and additional 67 cm to the calorimeter. The deterioration in BCAL performance by such modifications would not be justified by this additional photon coverage.

How large are these baryon resonance cross sections? The cross section measurements near GLUEX energies show significant Δ^{++} production in the 3-prong and 5-prong topologies but little Δ^+ or Δ^0 production. For example, in the 3-prong topology, the cross sections for $\rho^-\Delta^{++}$, $\rho^0\Delta^+$ and $\rho^+\Delta^0$ are 1.1 ± 0.2 μb, 0.3 ± 0.2 μb and 0.2 ± 0.2 μb respectively. The cross sections for $n\rho^0\pi^+$ and $\Delta^-\pi^+\pi^+$ are 2.0 ± 0.6 μb and 0.2 ± 0.2 μb respectively [26]. In the 5-prong channel with a single π^0, reactions with a Δ^{++} account for nearly 75% of that channel but no reactions with Δ^+ are quoted. Although measurements are based on low statistics, there appears to be little Δ^+ or Δ^0 production.

1.6 Photon energy and position resolutions

The ability to efficiently reconstruct π^0 and η mesons is what drives the requirements on photon energy and position resolutions that in turn determine the mass resolutions of the π^0 and η masses. To understand this interplay we generated events corresponding to the reaction $\gamma p \to \eta\pi^0 p \to 4\gamma p$ at $E_\gamma = 9$ GeV, with $\eta\pi^0$ mass distribution uniform in mass from 1 to 2 GeV/c^2 and uniform in angles with $t-$dependent production of $e^{-5\cdot|t|}$.

Energy resolution: The photon energies were smeared to follow the following resolution function[1]:

$$\frac{\sigma_E}{E} = \frac{a}{\sqrt{\mathrm{E(GeV)}}} \oplus b \tag{1.1}$$

For BCAL we use 0.054 GeV$^{-1/2}$ and $b = 0.01$, from GEANT simulations [27], which are also consistent with resolutions obtained with the KLOE calorimeter [1, 2] and with the beam tests of a BCAL 4-m module prototype [28]. The GEANT simulations, KLOE experience, and BCAL prototype tests will be described in

[1]From here on, in this Section and following Sections, we will assume the same form for the energy resolution and the constants a and b, which represent the *statistical* and *floor* contributions respectively, will be given either as a percent or fraction assuming that the energy E is given in units of GeV.

more detail below. For FCAL we use 0.073 GeV$^{-1/2}$ and $b = 0.036$, as obtained for the RadPhi calorimeter [5, 6].

Position resolution: For BCAL, we use the following resolution in $R\phi$ where R is the BCAL inner radius (65 cm) and ϕ is the azimuthal angle:

$$\delta(R\phi) = \frac{5 \text{ mm}}{\sqrt{\text{E(GeV)}}} \tag{1.2}$$

The above assumption is consistent with results of BCAL simulations [27] and with the proposed inner 2×2 cm^2 readout scheme for the ends of the BCAL modules. The polar angle, θ, resolution is assumed to be driven by the resolution in z along the BCAL fiber which in turn is driven by the resolution in time difference between the two ends of a BCAL module. We assume the timing resolution is given by:

$$\sigma_t(\text{ps}) = \frac{54}{\sqrt{\text{E(GeV)}}} \oplus 50 \tag{1.3}$$

and the resolution in z is given by $dz = \sigma_t \cdot v_{eff}/2$ where v_{eff} is the effective velocity of light in the fibers that takes into account the index of refraction and bounces ($v_{eff} = 0.53c$). With this:

$$\sigma_\theta = \frac{R}{R^2 + z^2} dz \tag{1.4}$$

Figure 1.10 shows the dependence of σ_θ as a function of θ for various photon energies.

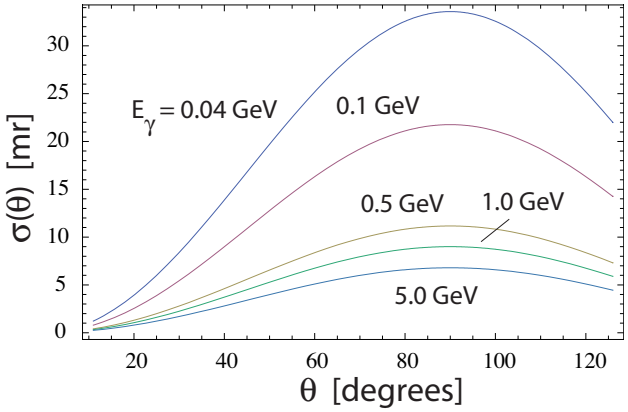

Figure 1.10: BCAL polar angular resolution as a function of angle for photon energies of 0.04, 0.1, 0.5 and 1.0 GeV.

For FCAL we assume a position resolution in the plane of FCAL to be [5].

$$\sigma_r = \frac{6.4 \text{ mm}}{\sqrt{\text{E(GeV)}}} \tag{1.5}$$

Mass resolutions: Given these assumptions as defining our *nominal* resolutions, we smear the photon energies and positions and compute the di-photon masses for the photons originating from the η decay and from the π^0. The resulting distributions, assuming nominal resolutions, are fit to a Gaussian and the widths obtained from these fits are plotted in Figure 1.11. Several cases are considered: (0) when both photons from the η or π^0 are in FCAL; (1) when both photons are in BCAL; (2) when one photon is in BCAL and the other in FCAL; and (3) any combination of FCAL/BCAL. We also considered, for any combination, degrading or improving the nominal resolution such (4) doubling the statistical term in the energy resolution;

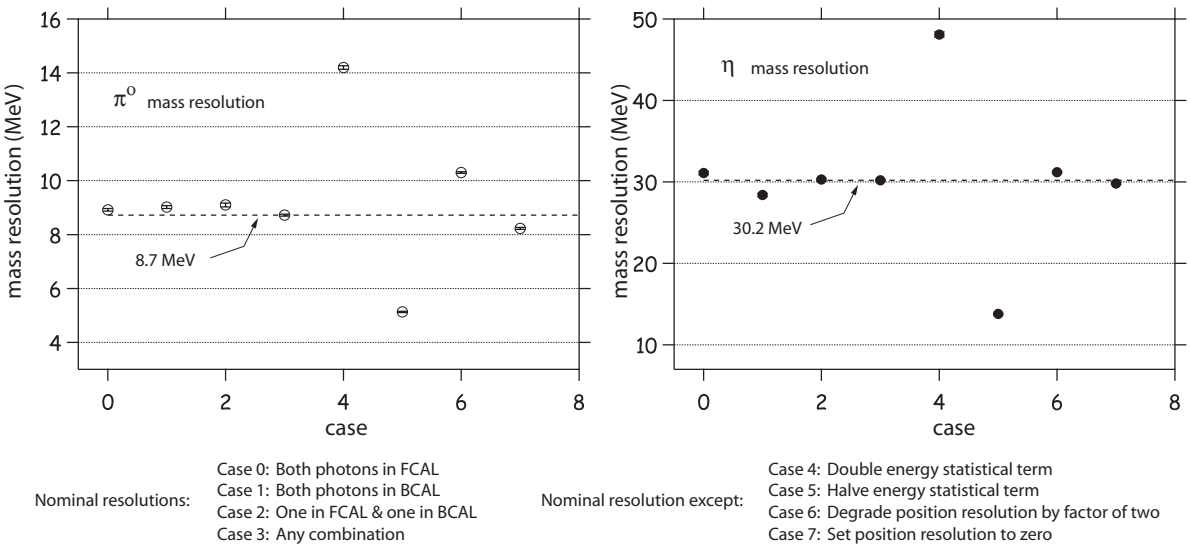

Figure 1.11: The π^0 and η mass resolutions obtained under different assumptions for energy and position resolutions in FCAL and BCAL.

(5) halving the statistical term in the energy resolution; (6) degrading the position resolution by a factor of two and (7) assuming perfect position determination. The mass resolutions for the η and π^0 are 30.2 MeV/c^2 and 8.7 MeV/c^2 respectively. By comparison the η and π^0 widths were measured as 30.8 ± 0.5 MeV/c^2 and 12.1 ± 0.1 MeV/c^2 respectively in E852 for the reaction $\pi^- p \to \eta\pi^0 n$ [29]. The mass resolution is primarily driven by the energy resolution and the mass resolution of the π^0 is more sensitive to the position resolution compared to the η.

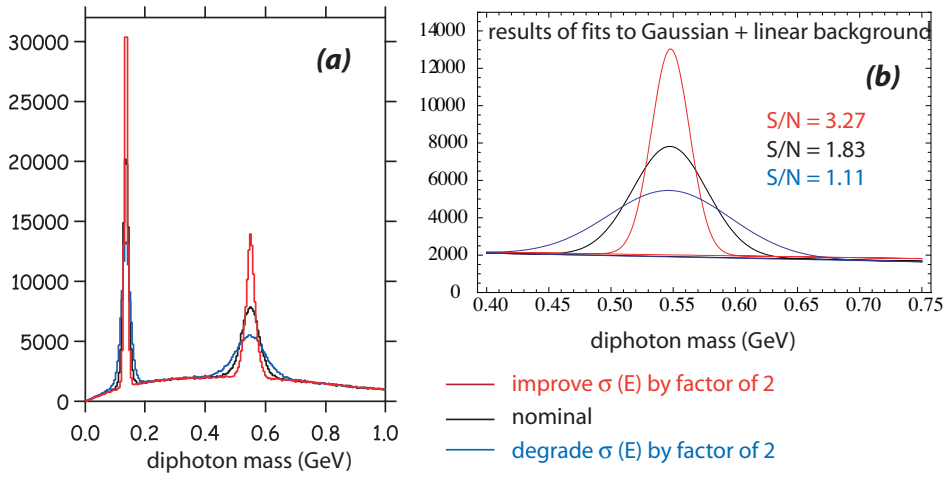

Figure 1.12: (a) The diphoton mass for the $\eta\pi^0$ reaction after resolution smearing using nominal resolutions (black), improving σ_E by a factor of two (red) and degrading σ_E by a factor of two (blue). There are six combinations per event. (b) Results of fitting the η mass region with a Gaussian and linear background. The background and signal were integrated over $\pm 2\sigma$ to obtain signal over noise S/N for the three resolution assumptions.

Figure 1.12 shows the diphoton mass for the $\eta\pi^0$ reaction with six entries per event after resolution smearing assuming nominal resolutions and degrading and improving the energy resolution by a factor of

two. Also shown are the results of fitting the spectrum near the η mass region to a sum of a Gaussian and linear background. Both signal and combinatoric background are integrated over $\pm 2\sigma$ to obtain an estimate of signal (S) over combinatoric background (N). In this study the combinatoric background in the four-photon sample comes from $\eta\pi^0$ events. The four-photon sample will also be populated by $\pi^0\pi^0$ events which will increase the combinatoric background depending on the relative cross-sections for these two final states. Kinematic fitting can be used to eliminate the $\pi^0\pi^0$ events from the four photon sample. This technique was used in the E852 experiment to study $\eta\pi^0$ final state [30] which has a cross-section about an order of magnitude lower than for the $\pi^0\pi^0$ final state in π-induced interactions. Another source feeding the four-photon sample will be final states with more than four photons where one of the photons is undetected or final states with fewer than four photons but with spurious additional photons either resulting from interactions in detector material or due to an artifact of the reconstruction software. These issues will be discussed in the section on studies with full detector simulations and reconstruction.

1.7 Momentum resolution and reconstruction efficiencies for charged particles

As discussed in section 1.4.2, charged particles are tracked through the detector using the CDC and FDC chambers. The CDC measures position normal to a wire to accuracy of about 150μm and through the use of $\pm 6^\circ$ stereo layers, can determine the position along the beam direction to an accuracy of about 1.5mm. The FDC measures positions of hits in the plane normal to the beam direction to an accuracy of about $200\,\mu m$, while the position in z is defined by how well the location and relative orientation of the chamber packages is known.

To determine the momentum resolution for charged particles in GlueX, the particles are tracked through the detector simulation (HDGeant [31],[32] using GEANT 3.14). This simulation contains our best estimates of all the material in GlueX as well as models for all relevant detector responses. The resulting events are then reconstructed using the GlueX reconstruction software [33]. The current software uses hits from the chambers with design resolutions to find and then fit the tracks. Both the Monte Carlo and the reconstruction software use a realistic field map for the solenoidal magnetic field including fringe fields out to the time-of-fligh wall.

To obtain the momentum resolution of GlueX, charged particles of a given momentum, $\vec{p}$, are generated and tracked through the detector. The fit momentum is then compared with the generated momentum. This leads to the resolution plots shown in this section. These studies map out the resolution of the detectors independent of the probability of the underlying physics producing such an event. In particular, there are large regions of the mapped resolution where there will be no physics events.

We start with the momentum resolution,

$$\sigma_{\Delta p/p} \quad = \quad \frac{\Delta \mid \vec{p} \mid}{\mid \vec{p} \mid} .$$

Figure 1.13 shows a scatter plot of $\sigma_{\Delta p/p}$ as a function of $\mid \vec{p} \mid$ (vertical axis) and polar angle θ (horizontal axis). Most of the plot shows a momentum resolution on the order of 1 to 2 %. Figure 1.14 shows a projection of 1.13 for several fixed values of total momentum in the range of 1 to $7\,GeV/c$. There are several structures in 1.14 which can be understood in terms of the geometry of detector. The degradation in resolution for very forward tracks is due to the little measured bending for these tracks which go roughly parallel to the magnetic field in GlueX . The bumps that occur on the 10° to 25° range correspond to particles not hitting all the FDC packages. A jump is observed each time a package is not hit. The rise in the backwards direction corresponds to particles missing the CDC—however this structure is in regions of phase space which have no events. In fact, most of the angular region beyond 40° will rarely see particles of momentum larger than $2\,GeV/c$. Most particles in this region will have a momentum resolution better than 1.5%.

We next look at the polar angle resolution,

$$\sigma_{\Delta\theta} \quad = \quad \Delta\theta .$$

Figure 1.15 is a scatter plot showing $\sigma_{\Delta\theta}$ in milliradians as a function of both $\mid \vec{p} \mid$ (vertical axis) and polar angle θ (horizontal axis. Figure 1.16 is a projection of the angular resolution for slices of polar angle θ going from 10° to 90°. Finally, the azimuthal angular resolution

$$\sigma_{\Delta\phi} \quad = \quad \Delta\phi .$$

is shown in Figures 1.17 and 1.18.

Track Finding: The current vesrion of the GlueX software starts with a track-finding package that looks for tracks in the CDC and FDC separately, and then tries to merge them. Figure 1.19 shows the track-finding efficiency for this package as a function of both total number of hits and which chambers the tracks are in. A track is considered found if the identified hits look reasonably similar to the generated track. The solid triangles show the track finding efficiency when only the FDC is used as a function of the poalr angle θ while the solid squares show the same plot for the CDC. The solid circles show the efficiency for finding either a

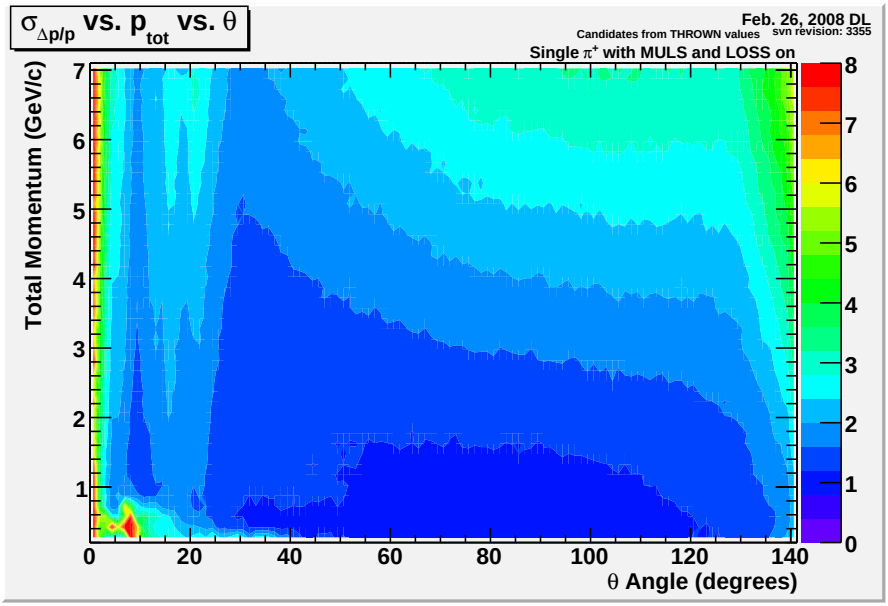

Figure 1.13: Total momentum resolution (%) as a function of the total momentum p and polar angle θ at the primary vertex.

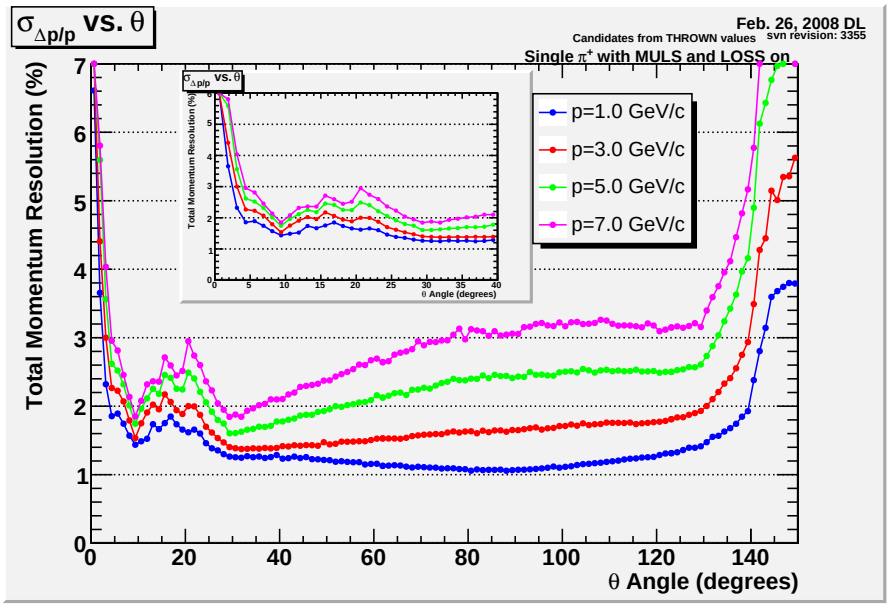

Figure 1.14: Total momentum resolution (%) as a function of the polar angle θ at the primary vertex for several values of momentum p. This plot is a projection of data in the scatter plot in Figure 1.13.

CDC or and FDC track. The colored regions labeled FDC and CDC map the number of hits on the track in the particular detector. Overall, there is very good track-finding effciecny in GlueẌearly 100% except for a small transition region near 12°. It is expected that as the track finding software continues to develop over the next five years that these efficiencies will impeove. We have also studied track-finding in the presence

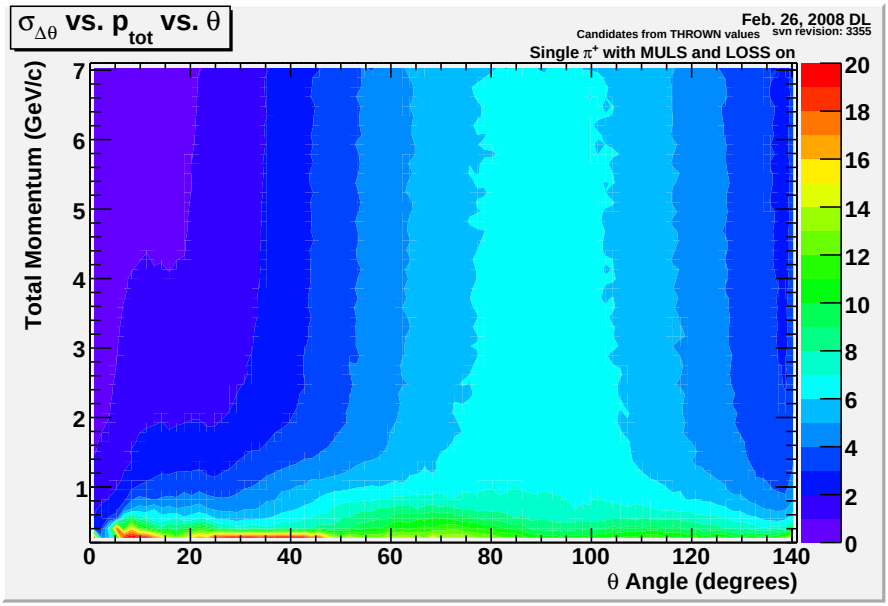

Figure 1.15: Polar angle resolution (mrad) as a function of the total momentum p for various polar angle θ at the primary vertex.

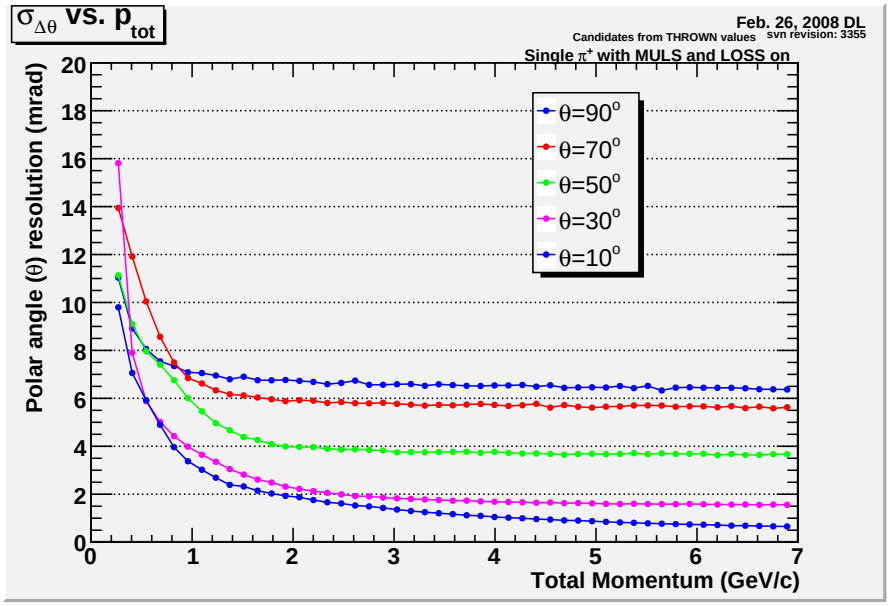

Figure 1.16: Polar angle resolution (mrad) as a function of the total momentum p for various polar angle θ at the primary vertex. This is a projection of Figure 1.15

of eletromagnetic backgrounds in GlueX.These show a small (few percent) degredation of the efficiencies shown in Figure 1.19.

After carrying out track finding, the tracks need to be fit to obtain particle information. This package has also been written, but as with track finding , we also anticpate that it will improve as we continue to

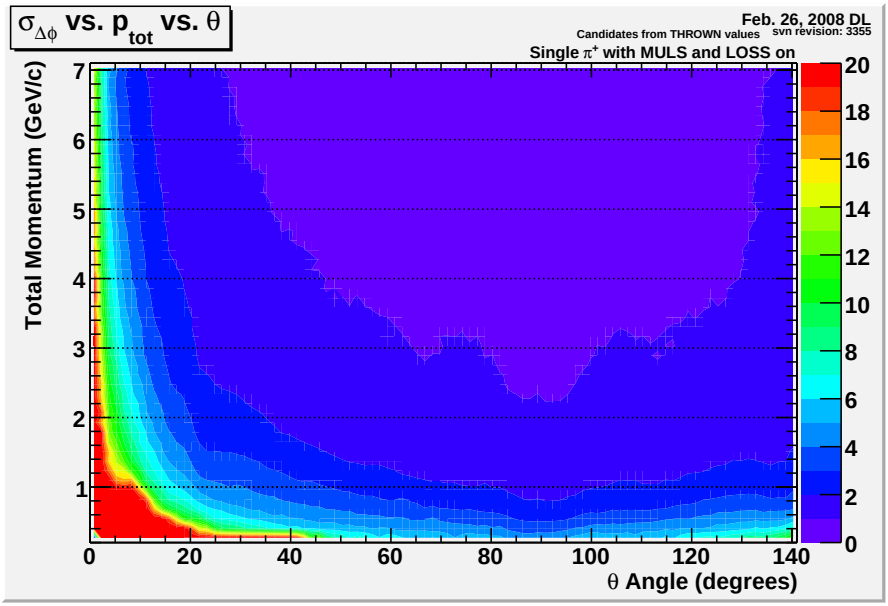

Figure 1.17: Azimuthal angle resolution (mrad) as a function of the total momentum p for various polar angle θ at the primary vertex.

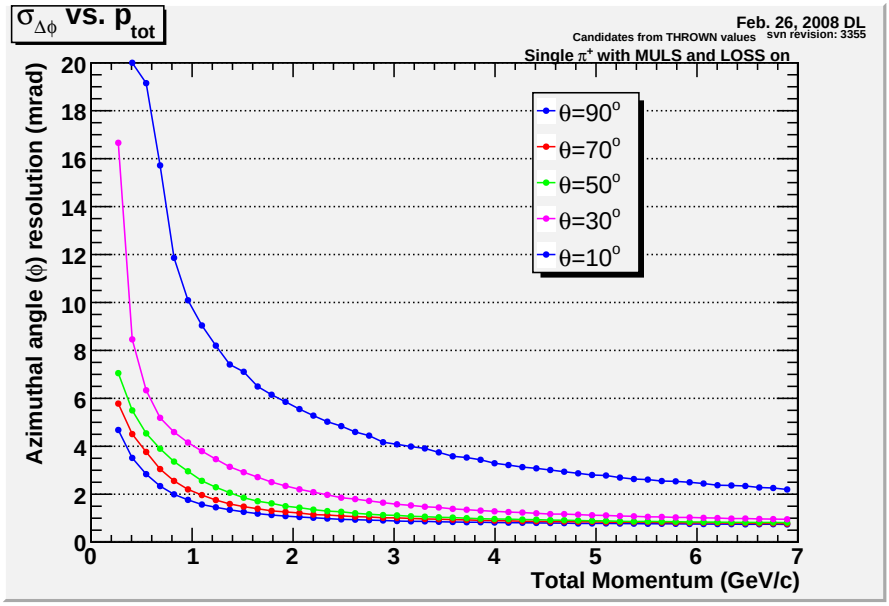

Figure 1.18: Polar angle resolution (mrad) as a function of the total momentum p for various polar angle θ at the primary vertex. This is a projection of Figure 1.17

develop it over the next five years. At the moment, it is able to fit about 85% of the found tracks. At the moment, the lost 15% appears to be related to pathologies in the fit that we anticipate can and will be resolved. We fully anticipate that the track fitting efficiency can be improved to be close to that for track finding in GlueX.

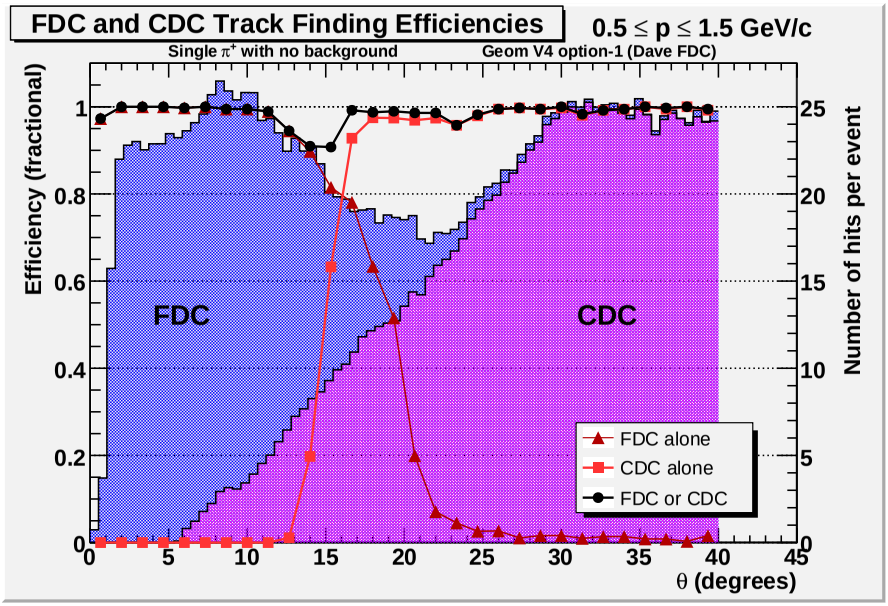

Figure 1.19: Track finding efficiency in the CDC and FDC, see text for explanation.

Parameterized Resolutions: Based on the resolutions obtained from HDGEANT and the GlueX reconstruction software, we have developed a set of parametrized resoltution and acceptance functions which can be used to carry out more sophisticated analysis projects in GlueX. An example of these are the amplitude analysis studies in section 1.10.

1.8 Mass resolutions involving charged particles and photons

To compare the contributions of charged particle resolution and photon resolutions to narrow width particles, as in the decays $\eta \to \pi^+\pi^-\pi^0$, $\omega \to \pi^+\pi^-\pi^0$ and $\phi \to \pi^+\pi^-\pi^0$ we studied the reaction $\gamma p \to \phi p$. For this study, the distribution in $|t|$ followed $e^{-|t|/2}$ to provide a mix of charged particle momenta that would include more lower momentum particles. The ϕ was generated with a mass and width of 1020 and 4 MeV/c^2 respectively. The photon energies and angles were smeared according to the nominal resolutions discussed above. The charged particle four vectors (for the $\pi^\pm$) were smeared to follow the momentum error and angular error plots generated in a study of track finding in GlueX [33]. The plots shown in the referenced study were fit to analytical forms. These plots were generated before the material associated with the CDC and FDC tracking chambers was reduced so in what follows we consider the nominal charged particle resolutions and resolutions improved by a factor of two. The effect of the resolution smearing on the observed width of the ϕ is shown in Table 1.8. The distribution in the square of the missing mass recoiling against the ϕ is shown in Figure 1.20 under various assumptions of four-vector smearing.

Condition	Nominal errors for $\pi^\pm$	Nominal errors/2 for $\pi^\pm$
Photon smearing only	14.8 ± 0.1 MeV/c^2	14.8 ± 0.1 MeV/c^2
Charged particle smearing only	16.7 ± 0.1 MeV/c^2	11.1 ± 0.1 MeV/c^2
Both smeared	22.2 ± 0.2 MeV/c^2	17.6 ± 0.1 MeV/c^2

Table 1.8: Observed width for the ϕ, generated with a width of 4 MeV/c^2, after four-vector smearing.

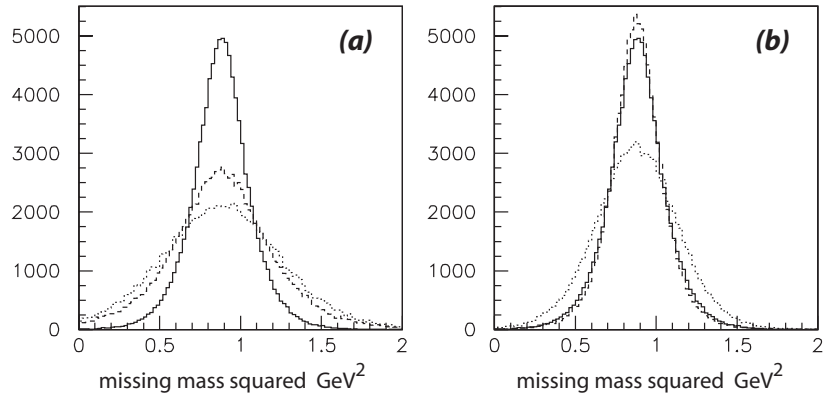

Figure 1.20: Missing mass squared recoiling off the ϕ for the reaction $\gamma p \to \phi p$ with photon smearing only (solid histogram), charged particle smearing only (dashed) and both (light dashed) for nominal charged particle smearing (a) and smearing reduced by a factor of two (b).

1.9 Particle Identification in GlueX

Separation of pions, kaons, protons and possibly electrons will be necessary to carry out the entire GlueX physics program. In order to do this, a comprehensive system of particle identification and analysis will be needed. In GlueX , this system will be staged in two parts—the first as part of the base-line detector and the second as an additional detector system that would come on line at a later time. As with most particle identification systems, these are somewhat redundant with each other. In addition to the hardware, we also anticipate sophisticated analysis that will look globally at an individual event to identify the best possible particle assignments consistent with all information.

In GlueX , the base-line hardware systems consist of a time-of-flight wall just in front of the FCAL which will measure times with a 70 ps accuracy and will see charged particles in a roughly 11° degree wide cone

about the beam axis. Additional information will come from timing measurements in the BCAL and possibly energy deposition from charged particles in the BCAL. Finally, the CDC will measure dE/dx information that will be useful for particles below $0.45\,GeV/c$ momentum.

The upgrade option for GlueX is a ring imaging Cerenkov counter (RICH) located in front of the time-of-flight wall. Such a detector would allow excellent particle identification for particles with momentum up to about $6\,GeV/c$. Space has been left in the detector design for this upgrade.

1.9.1 Time of flight information

As noted above, information about the time difference between the two ends of the BCAL module photosensor readout provides the impact point (z-position) of photons striking the inner surface of BCAL. The average time, or mean time, of the two ends can be used to provide time of flight information that may be used for particle identification. The time difference is relevant and crucial for determining the four-vector information for photons.

The mean time information could, in principle, be used for particle identification for hadrons, in particular in providing π/K or π/p separation. As will be discussed in what follows, the mean time resolution obtained from cosmic ray (minimum ionizing particle) measurements with a 4 m module, is approximately 500 ps. This time resolution is inadequate for π/K separation but can be used for π/p separation.

We generated events to simulate the reaction $\gamma p \rightarrow \pi^+\pi^-\pi^0 n$ where the 3π result from the decay $a_2(1320) \rightarrow \rho\pi$ or $\pi_2(1320) \rightarrow f_2\pi$ with a $e^{-5\cdot|t|}$. The charged particles were tracked through a uniform magnetic field and for $\pi^\pm$ reaching BCAL the π/K difference was computed. The time difference distribution is shown in Figure 1.21(a). Clearly, a 500 ps mean-time resolution does not allow for π/K separation. For protons reaching BCAL, we compute the π/p time difference divided by 500 ps. The resulting distribution is shown in Figure 1.21(b). About 77% of the events where the proton track has sufficient transverse momentum to reach BCAL have a $(t_p - t_\pi)/\sigma_t > 4$.

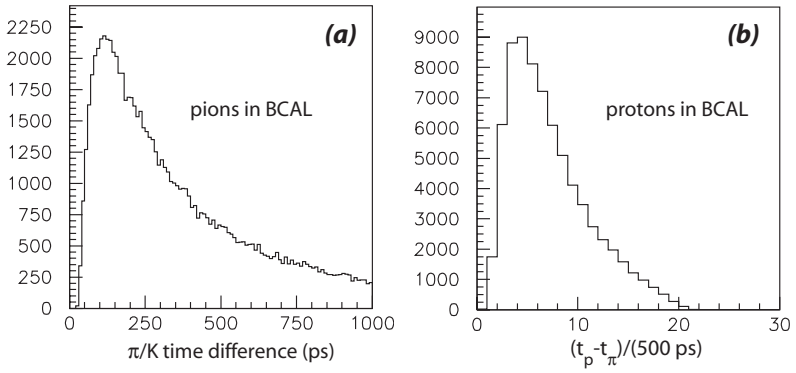

Figure 1.21: (a) The distribution in π/K time difference for $\pi^\pm$ reaching BCAL from the reaction $\gamma p \rightarrow \pi^+\pi^+\pi^- p$; (b) For protons reaching BCAL, the proton/pion time difference divided by 500 ps, the assumed mean time resolution for BCAL for minimum ionizing particles.

1.9.2 dE/dx in the CDC

The CDC will provide dE/dx information for charged particles. Given the fact that the path length in a straw is not a constant, this is more difficult than in a conventional drift chamber, however, it has been done [34]. For GlueX, the particles of interest have total momentum less than 0.45GeV/c, and are thus unlikely to be seen in any other particle identification system. Several studies have been done to look at the energy deposition in the straws from pions, kaons and protons. The results of these are summarized in

Figure 1.22. The left-hand plot shows particles moving at a polar angle of 90° in GlueX. For such particles, those with total momentum less than 0.25GeV/c will spiral and miss the BCAL. We also note that while none of the protons with momentum so low will be detected (see Figure 1.9), higher momentum protons will be slowed down to fall into this momentum range. For such particles, there is very good separation between all three particle species.

The right-hand plot in Figure 1.22 shows the same dE/dx calculation for particles moving forward at 15°. Here we consider particles lower than 0.45GeV/c and we see that while the π-K separation may be difficult, we should be able to carry out excellenr π-p separation.

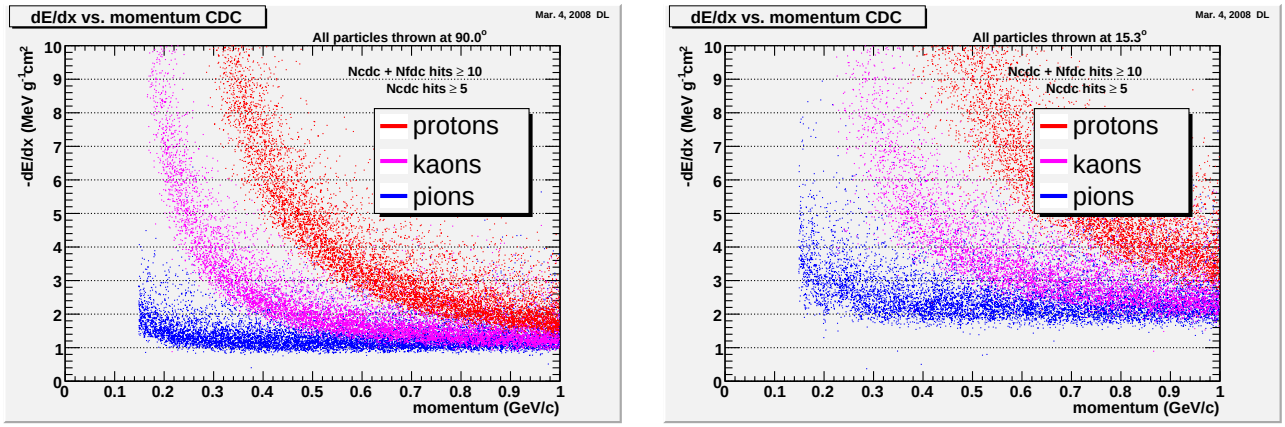

Figure 1.22: Expected energy loss as a function of particle momentum in the CDC, taking into account of the path length in each CDC straw. (left) Tracks going at 90° in the lab. (right) Tracks going at 15° in the lab. Very good π-p separation is seen for track momentum below $0.5\,GeV/s$, while less significant π-K separation will be possible.

1.9.3 Global Event Analysis

Individual particle identification systems provide a most probable assignment to for particle type based on information in a single detector. Physics principles such as strangeness conservation in conjunction with analysis tools such as kinematic fitting can be used to make global particle assignments to all particles in an event. Studies carried out with realistic resolutions in GlueX in conjunction with kinematic fitting have been carried out [35]. This looks at the following two reactions in GlueX to deterine what can be done with global fitting.

$$\begin{aligned} \gamma p &\rightarrow p K^+ K^- \pi^+ \pi^- \\ \gamma p &\rightarrow p \pi^+ \pi^- \pi^+ \pi^- \end{aligned}$$

The first is a signature reaction, while the second is a fairly prolific final state in GlueX. The two were generated in ratio of 1 in 100 which roughly follows the known cross sections. The studies also included intermediate resonances in various two-meson sub systems.

When no particle identification is assumed, there are 15 ways to make particle assignments in the final state. With a positive cut at 10% confidence level on the correct hypothis and a rejection of the wrong hypothesis at the 10% confidence level, we find that about 45% of the true signal survive and 1% of second reaction survives. This leades to a spectrum that has about twice as much background as true signal. If we then extend this study to include the situation where the proton has been positively identified in one of the GlueX syetems, the combinatorics falls from 15 to 5 and the amount of background leaking through goes down by another order of magnitude with the accepted background now representing about 8% of the accpeted signal. However, this requires that we reject roughly 55% of the true signals.

As we continue this by including a probabalistic time-of-flight measurement, the acceptance for true signal goes up and the background rejection conyinues to improve.

1.10 Expectations for amplitude analyses

The ultimate goal of the GlueX experiment is to identify exotic mesons by an amplitude analysis of exclusive final states. The sensitivity of the amplitude analysis, *i.e.* how small a signal can be detected, depends on having sufficient statistics and how well systematics, both from the experiment and from the analysis, are controlled. GlueX collaborators have recently been awarded an NSF grant to develop tools for understanding the phenomenological systematics inherent in an amplitude analysis. To estimate the sensitivity we expect from GlueX requires a full simulation of the detector response to real and background events, charged particle and photon reconstruction, kinematic fitting to identify exclusive final states and finally the actual amplitude analysis. Work is in progress and the last section of this report summarizes results from the first steps along this program.

In the meantime, we can turn to results of analyses from experiment E852 at Brookhaven. Data were collected from $\pi^- p$ interactions at 18 GeV/c leading to the final states $\pi^-\pi^0\pi^0 p$ and $\pi^-\pi^-\pi^+ p$ [36]. That experiment used the multiparticle spectrometer (MPS) at the AGS and utilized a lead glass calorimeter on which the FCAL design is based. Figure 1.23 shows the results of an amplitude analysis for the $J^{PC} = 2^{++}$ and $J^{PC} = 4^{++}\rho\pi$ amplitudes. Two well-established meson states are observed in these amplitudes, the tensor state $a_2(1320)$ in the former and the spin-4 state $a_4(2040)$ in the latter. The intensity of the a_4 is about 3% that of the a_2 and the amplitude of the a_4 is similar for the $\pi^-\pi^0\pi^0$ and $\pi^-\pi^-\pi^+$ systems, even though the experimental systematics for these two modes are very different.

How do GlueX and E852 compare? The resolutions obtained for the π^0 mass resolutions for GlueX calorimetry are similar to those obtained in E852. Studies are underway to estimate the charged particle momentum and angle resolutions. The $\pi^-\pi^-\pi^+$ and $\pi^-\pi^+$ effective mass distributions and distribution in momentum transfer from incoming beam to outgoing 3π system observed in E852 were used to generate a Monte Carlo event sample of a similar final state for 9 GeV photoproduction. Charged particle momenta and angles were smeared using current best-estimate resolution functions and the result was that the resolution in the square of the missing-mass recoiling against the 3π system for GlueX will be at least as good as that in E852. This would indicate that the ability to kinematically identify exclusive reactions should also be at least as good.

1.10.1 A signature reaction: $\gamma p \to \eta\pi^0 p$

We now turn to one of the signature reactions for GlueX, the reaction $\gamma p \to \eta\pi^0 p$. This reaction is of particular interest for exotic hybrid searches since the $\eta\pi^0$ has well-defined charge conjugation quantum number ($C = +$) and if the η and π^0 resonate in a $P-wave$ then the resonance has exotic $J^{PC} = 1^{-+}$. For events with uniform $\eta\pi^0$ masses between 1.0 and 2.0 GeV/c^2, uniform in decay angles, and produced with a $e^{-5\cdot|t|}$ distribution, the photons populate the calorimeters, the beam hole in FCAL and the angular region $> 126°$ as shown in Table 1.9. For completeness we include the photon population for PYTHIA events as well as for the recoil baryon resonance production $\gamma p \to X\Delta \to X\pi^0 N$. The latter reaction will be discussed in more detail below.

Table 1.10 shows the fraction of accepted (no photons in beam hole or with angles $> 126°$) events that have both photons from the η or π^0 in FCAL or BCAL or shared between FCAL and BCAL.

Figure 1.24 has information about the photons hitting BCAL. The variable z is the distance along the inner surface of BCAL starting from the upstream end at $z = 17$ cm and ending at the downstream end at $z = 407$ cm. The 30-cm target center is at $z = 65$ cm. The histogram is the distribution of the photons along z (use the left vertical scale) while the dashed curve (use the right vertical scale) is the integral fraction of photons in percent. For example, 30% of the BCAL photons hit between $z = 17$ cm and $z = 212$ cm, the upstream half of BCAL. The other curves also use the right vertical scale. The green curve is the number of BCAL radiation lengths intercepted by the photon trajectory assuming a 1.45 cm radiation length for the Pb/SciFi matrix. The cusp at $z = 312$ cm corresponds to a photon angle of 14.7° where the number

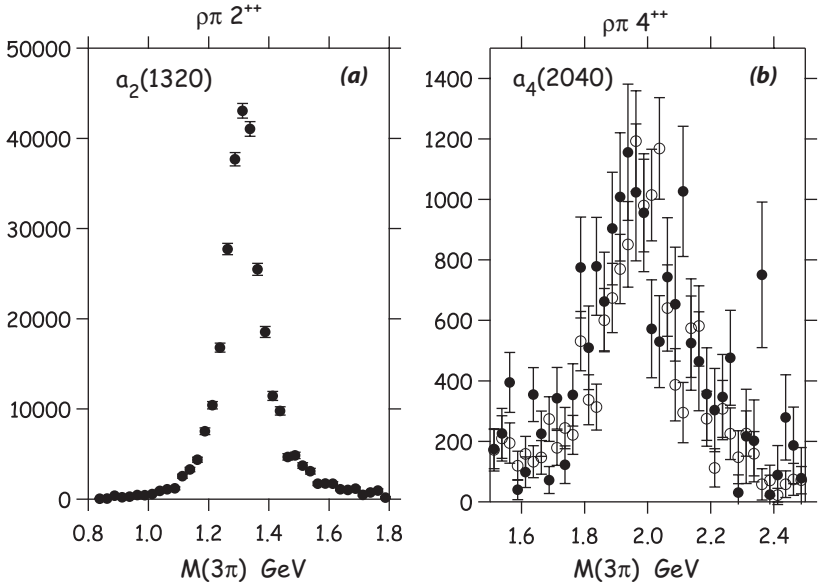

Figure 1.23: (a) Results of an amplitude analysis of data from $\pi^- p$ interactions at 18 GeV/c leading to the final states $\pi^-\pi^0\pi^0 p$ and $\pi^-\pi^-\pi^+ p$ from Brookhaven experiment E852 [36]. Results are shown for the (a) $J^{PC} = 2^{++}$ and (b) $J^{PC} = 4^{++}\rho\pi$ amplitudes. Filled circles are for the $\pi^-\pi^0\pi^0$ system and unfilled for the $\pi^-\pi^-\pi^+$ system. In (a) the tensor state $a_2(1320)$ is observed and in (b) the well-established spin-4 $a_4(2040)$ is seen. Note that the intensity of the a_4 is about 3% that of the a_2.

Element	Percent of all photons PYTHIA Events	Percent of all photons $\eta\pi^0$ Events	Percent of all photons $X\Delta$ Events
Angles $> 126°$	1.7	0.20	7.8
BCAL	70.5	45.68	89.8
FCAL	27.3	53.15	2.4
Hole in FCAL	0.5	0.97	0

Table 1.9: Fraction of all photons populating the GLUEX calorimeters, the angular region $> 126°$ and the beam hole in FCAL for PYTHIA events and $\eta\pi^0$ events.

of radiation lengths is 68. As the photon angle changes from 10.8° to 14.7° (see Figure 1.1), the number of radiation lengths intercepted by the photon trajectory increases from 0 to 68. In this angular region the photon trajectory exits out the downstream end of BCAL. How well these photons can be constructed, using GEANT-based simulations and photon reconstruction software, will be discussed later. The cusp at $z = 30$ cm corresponds to a photon angle of 118.1°. The minimum of the green curve is at $z = 65$ cm or at 90° corresponding to 17 radiation lengths (the module is 22.5 cm thick). The blue curve shows the photon angle as a function of z.

1.10.2 Amplitude analysis and understanding of acceptance

As seen in Figure 1.24, the angular region between 10.8° and 14.7° (see Figure 1.1) has a significant population of photons for events of the reaction $\gamma p \to Xp \to \eta\pi^0 p$. In this region there was a fair amount of material due to cabling associated with the FDC drift chambers in the original design, but recent changes have resulted in a significant reduction of material. The impact of remaining FDC material on photon reconstruction is currently under study. How well one understands the reconstruction efficiency in this region is critical for

Element	η	π^0
Both photons in FCAL	27%	46%
Both photons in BCAL	20%	35%
Photons in FCAL and BCAL	53%	19%

Table 1.10: Fraction of accepted $\eta\pi^0$ events that have photons from either the η or π^0 both in BCAL or FCAL or shared.

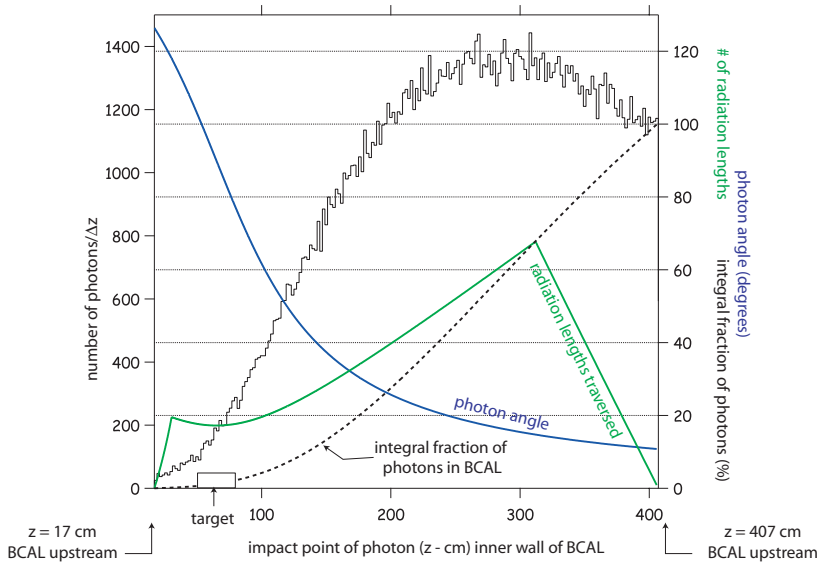

Figure 1.24: Histogram: Distribution of photons from the $\gamma p \to \eta\pi^0 p$ reaction along the inner wall of BCAL. The upstream end of BCAL is at $z = 17$ cm and the downstream end at $z = 407$ cm. Use the left vertical scale for the histogram. The three curves (all as a function of z) use the right vertical scale. The black dashed curve is the integral fraction of photons in BCAL in percent. The blue curve is the photon angle in degrees measured with respect to the beam (or with respect to the inner surface of BCAL). The green curve is the number of radiation lengths traversed by a photon.

the amplitude analysis. To illustrate this, we generate events with a uniform population of decay angles in the X rest frame. A frame that is often chosen is the Gottfried-Jackson frame where the polar angle, θ_{GJ}, is the angle between the momentum vector of one of the decay products (the η in our case) and the momentum vector of the beam, all in the X rest frame. A uniform decay angular distribution corresponds to a distribution flat in $\cos\theta_{GJ}$. The amplitude analysis fits the observed distribution in $\cos\theta_{GJ}$ to a sum of various waves corresponding to the angular momentum L between the η and π^0 and its projection M along the $z-$axis.

In Figure 1.25 we show the effect on the $\cos\theta_{GJ}$ distribution if we eliminate $\eta\pi^0$ events if one of the four photons from the event enters an angular region defined by the LAB angle θ. For distribution (I) no requirement was imposed. For distribution (II) the angular cut imposed extends from $\theta = 10.8°$ to $\theta = 11.7°$. For distributions (III) through (V), the lower limit remained the same while the upper limit was increased in $1°$ increments, up to $\theta = 14.7°$ for distribution (V). Also shown are the percentage of events that survive the various angular cuts along with the forward-backward asymmetry defined as $(F - B/(F + B)$ where F is the number of events with $\cos\theta_{GJ} > 0$ and B is the number of events with $\cos\theta_{GJ} < 0$. The imposition of the angular cut impacts the acceptance and sculpts the observed angular distribution. As noted above, if the $\eta\pi^0$ resonates in a P-wave ($L = 1$) the resonance has exotic quantum numbers. There are resonances with $L = 0$ and $L = 2$ that decay into $\eta\pi^0$ and an even-wave odd-wave interference will lead to a forward-backward

asymmetry in the $\cos\theta_{GJ}$ distribution. So a poorly understood acceptance in the critical angular region between BCAL and FCAL can lead to false amplitude analysis conclusions.

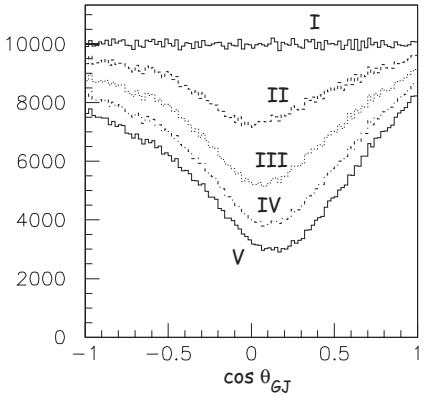

Case	Acceptance (%)	(F-B)/(F+B)
I	100	0.0
II	85	-0.01
III	73	-0.03
IV	63	-0.06
V	55	-0.08

Figure 1.25: The distribution in $\cos\theta_{GJ}$ for $\gamma p \to Xp \to \eta\pi^0 p$ events. For distribution (I) no cuts are imposed. For distributions (II) through (V), events are eliminated if one of the four photons enters various angular ranges as defined in the text. The corresponding acceptances and forward-backward asymmetries are also given.

1.10.3 Another signature reaction: $\gamma p \to b_1(1235)\pi p$

An important parameter for BCAL is the energy of the lowest energy photon that can be reconstructed. To understand the challenge we look at $\gamma p \to b_1^+\pi^0 n$ where the intermediate final state is $\omega\pi^+\pi^0$ and the final state is $\pi^+\pi^+\pi^-\pi^0\pi^0 p$. In this note we look at the kinematics of a 2 GeV/c^2 state decaying into $b_1\pi$. The incident photon energy is assumed to be 9 GeV. This is one of our signature reactions for exotic hybrid searches and yields four photons.

The plot of Figure 1.26(a) shows the energy spectrum of the lowest energy photon in the event. The plot of Figure 1.26(b) shows the fractional running integral, so, for example, 25% of the events have a photon with energy less than 80 MeV. The scatterplot of Figure 1.27 shows the energy versus angle for the lowest energy photon in the event for $\gamma p \to b_1^+\pi^0 n$. This scatterplot shows the challenge for this lowest energy photon reconstruction. Most of the low energy photons occur near the edge of BCAL where reconstruction is a challenge due to presence of material at that location.

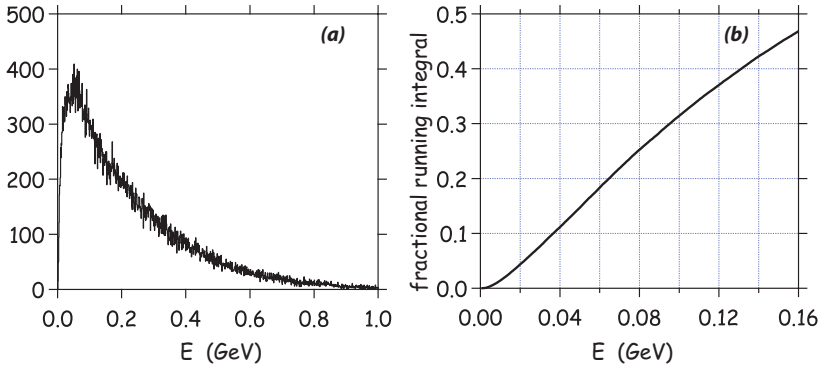

Figure 1.26: Left: Spectrum of lowest energy photon in a $\gamma p \to b_1^+\pi^0 n$ event; Right: Fractional running integral for the plot to the left.

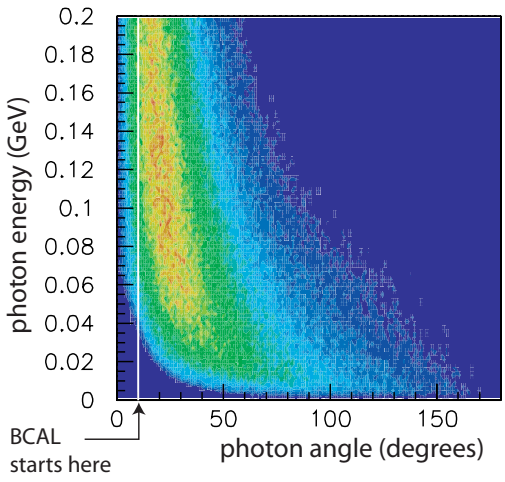

Figure 1.27: Energy versus angle for the lowest energy photon in the event for $\gamma p \to b_1^+ \pi^0 n$.

1.10.4 A signature reaction: $\gamma p \to 3\pi p$

There is a substantial literature on the decay of exotic mesons decaying to 3π final states with the most recent analysis of Brookhaven E852 data presented in reference [36]. While the existence of an exotic state at a mass of $1.6\,GeV/c^2$ which decays to three pions is somewhat in question, the partial wave analysis carried out in that reference stands as a benchmark as to what can be done. In particular, Figure 1.28 shows the results for two partial waves of an amplitude analysis of the final states $\pi^-\pi^-\pi^+$ and $\pi^-\pi^0\pi^0$. In particular, the analysis was able to pull out the signal for the spin-4 $a_4(2040)$ at a level of a few percent of the strong spin-2 $a_2(1320)$. In this regard, we take the capabilities of E852 as a benchmark in ones ability to extract small signals in an amplitude analysis.

Continuing with the 3π reaction, we show in Figure 1.29 various distributions from the three pion system. In the right-hand plots are for E852 using an $18\,GeV/c$ π^- beam to examine $\pi^- p \to \pi^-\pi^-\pi^+ p$ and in the left-hand plots, the simulated GlueX detector looking at the reaction $\gamma p \to n\pi^+\pi^+\pi^-$ for 8.5 to $9.0\,GeV$ photons. For the case of GlueX one a finite number of t-channel produced resonances were included. In looking at the plots, the overall distributions look quite similar, and while what are seen are not particularly narrow resonances, the structures look very much the same. Proceeding with this comparison, we have found that the widths of narrow resonances reconstructed in E852 and those in GlueX are quite similar, with the GlueX typically having somewhat narrower widths. Overall, we find that with the design resolutions of GlueX ,we are able to reconstruct things at least as well as was carried out in E852, and thus we should be able to carry out an amplitude analysis with at least the same level of precision.

Going beyond this, there have a been a number of studies using the simulated GlueX data to carry out specific amplitude analysis studies. The earliest of these is reported in reference [37] and reports on a double-blind study of the 3π reaction. This work used a parameterized Monte Carlo (MCFast[2]). In this first study, a linearly polarized photon beam using an unknown cocktail of t-channel generated mesons which decay to 3π was produced. These events were then given to the analysis team who carried out an analysis similar to that done by E852. In the end, the team found the seven amplitudes included in the generator and excluded about ten other amplitudes based on no observed signal at the sub percent level. This original study was later extended by degrading the detector performance at the level of detector resolution, gaps in the detector, and distorted magnetic fields [38]. This latter study indicated that at the level things were

[2]The MCFast program was written at FermiLab for use by the BTeV experiment. It allowed for both fast simulation and pseudo reconstruction of events with the ability to input reconstruction efficiencies and to get good estimates of reconstruction errors. The GlueX amplitude analysis work was carried out while one of the developers of the code was on the faculty of CMU. After the BTeV experiment was cancelled, the support for the package ended and with rapid changes in compilers and software, it quickly became nearly impossible to maintain and was dropped as a GlueX package in late 2004.

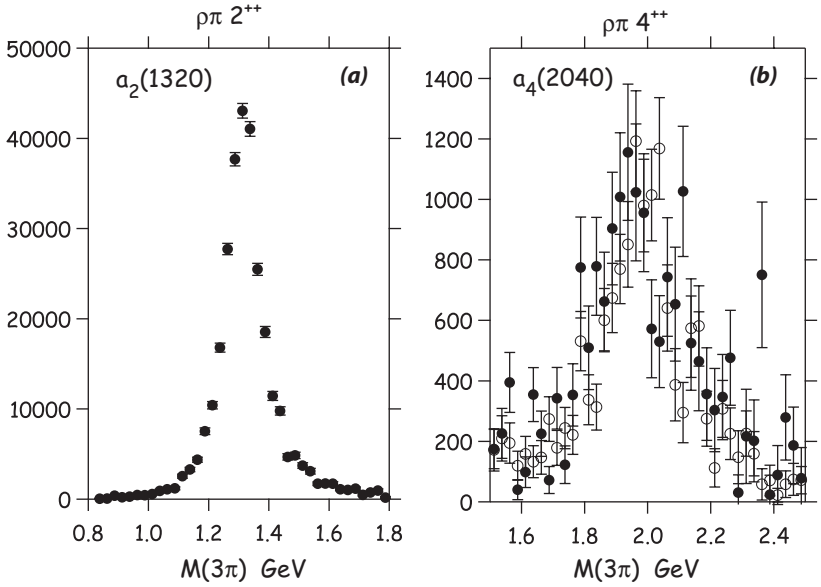

Figure 1.28: (a) Results of an amplitude analysis of data from $\pi^- p$ interactions at 18 GeV/c leading to the final states $\pi^-\pi^0\pi^0 p$ and $\pi^-\pi^-\pi^+ p$ from Brookhaven experiment E852 [36]. Results are shown for the (a) $J^{PC} = 2^{++}$ and (b) $J^{PC} = 4^{++}\rho\pi$ amplitudes. Filled circles are for the $\pi^-\pi^0\pi^0$ system and unfilled for the $\pi^-\pi^-\pi^+$ system. In (a) the tensor state $a_2(1320)$ is observed and in (b) the well-established spin-4 $a_4(2040)$ is seen. Note that the intensity of the a_4 is about 3% that of the a_2.

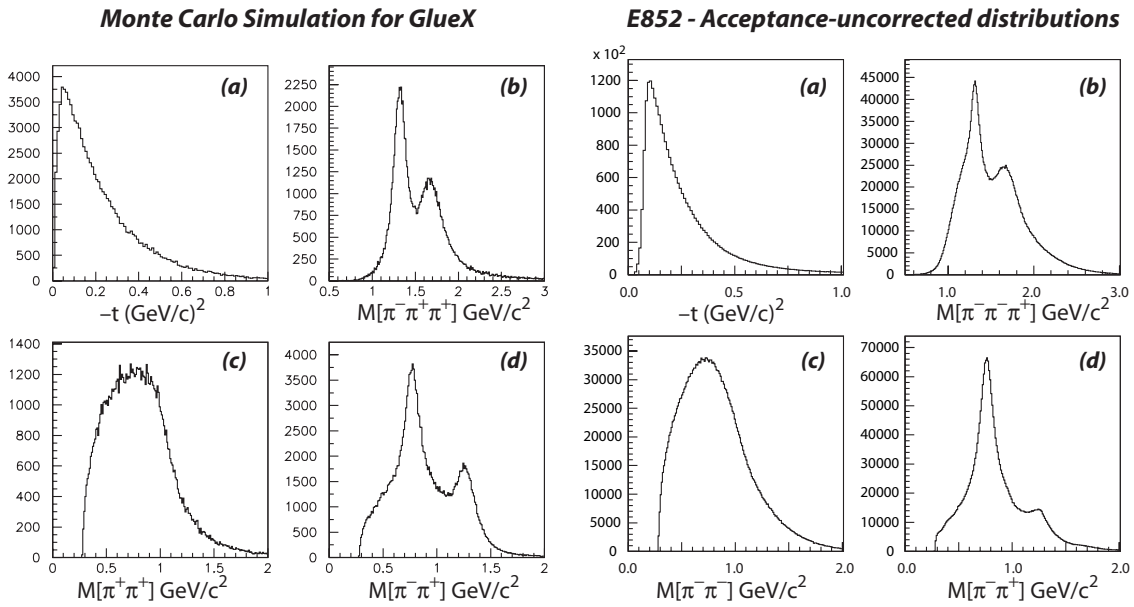

Figure 1.29: Physics distributions for the 3π final state. The left-hand plots are for simulated GlueX $\pi^+\pi^+\pi^-$ data while the right hand plots are for E852 [36] $\pi^-\pi^-\pi^+$ data.

simulated, the analysis results were robust against degradations of the detector.

Since those original studies, a realistic (GEANT-based) simulation of the GlueX detector and recon-

struction software have been developed. In particular, concerns have been raised that the original studies over-estimated the effects of realistic tracking software. This software has been discussed in section 1.7 and its performance is quite similar to the results obtained from the early fast simulations. We have also developed new fast simulation tools based on the performance of the GlueX software that are now used to carry out studies. One of these studies is to reproduce the original 3π amplitude analysis work. However, given the performance of the actual GlueX software, most of the results of the earlier amplitude analysis studies are still valid. The key point of those studies are that with the detector resolutions and performance and using realistic reconstruction software, it is possible to carry out an amplitude analysis that is sensitive to reactions that are only a few percent of a given final state.

1.11 Conclusions

1. Complete detection of final states involiving charged particles and photons are necessary for carrying out the broad program in gluonic excitation planned for GlueX.

2. The detection and measurement of π^0 and η mesons with adequate acceptance and resolution is essential for mapping the spectrum of exotic hybrid mesons.

3. Photoproduction at 9 GeV is expected to provide a rich hunting ground for exotic mesons. What little data on photoproduction exists at these energies provides almost no information on final states with multi-neutrals.

4. Fixed target photoproduction imposes a solenoidal geometry for the detector (see Figure 1.1), including cylindrical tracking (CDC) and calorimetry (BCAL) and circular planar tracking (FDC) and calorimetry (FCAL).

5. Calorimeters with requirements similar to BCAL and FCAL have been built and operated. The KLOE calorimeter provides guidance for BCAL and the lead glass calorimeter used in E852 and RadPhi provides guidance for FCAL.

6. The tracking specifications for the CDC and FDC allow us to reconstruct charged particles and make cuts on event purity that are at least as goos as other successful spectroscopy experiments.

7. A version of pythia, tuned to agree with what is known about photoproduction at GlueX energies, provides us with guidance on the angular and energy spectra of photons illuminating BCAL and FCAL. These studies indicate that the planned coverage and granularity are adequate.

8. Simulations of GlueX signature reactions leading to final states such as $\eta\pi^0 p$, $b_1\pi p$, ϕp and $3\pi p$ provide guidance on what is required for energy threshold and energy and position resolution for photons and momentum resolution for charged particles.

9. Achievable mean-time resolution for BCAL is adequate for π/p separation but not for π/K separation.

10. The overall particle identification system in conjunction with global fitting is suffcient to carry out the part of the GlueX exotic program involving non-strange final states and to start looking at some final states with kaons.

11. The ultimate identification of final states with strange particles will involve an addition Cherenkov detector (probably RICH) downstream of the FDC packages but in front of the time-of-flight wall.

References

[1] M. Adinolfi et al. The KLOE electromagnetic calorimeter. *Nucl. Instrum. Meth.*, A482:364–386, 2002.

[2] Hi Wally -

I will most likely be driving to Jefferson lab at that time. Can we do it during the lunch or coffee breaks of the GlueX workshop on either Thursday or Friday?

thanks – Curtis M. Adinolfi et al. The KLOE electromagnetic calorimeter. *Nucl. Instrum. Meth.*, A494:326–331, 2002.

[3] B. B. Brabson et al. A study of two prototype lead glass electromagnetic calorimeters. *Nucl. Instrum. Meth.*, A332:419–443, 1993.

[4] R. R. Crittenden et al. A 3000 element lead-glass electromagnetic calorimeter. *Nucl. Instrum. Meth.*, A387:377–394, 1997.

[5] R. T. Jones et al. A bootstrap method for gain calibration and resolution determination of a lead-glass calorimeter. *Nucl. Instrum. Meth.*, A566:366–374, 2006.

[6] R. T. Jones et al. Performance of the RADPHI detector and trigger in a high rate tagged photon beam. *Nucl. Instrum. Meth.*, A570:384–398, 2007.

[7] C. A. Meyer and Y. van Haarlem. The GlueX Central Drift Chamber. Technical report, GlueX Document, 2008. GlueX-doc-990-v5.

[8] D. S. Carman and S. Taylor. Forward Drift Chamber Technical Design Report. Technical report, GlueX Document, 2007. GlueX-doc-754-v5.

[9] Gunnar S. Bali et al. Static potentials and glueball masses from QCD simulations with Wilson sea quarks. *Phys. Rev.*, D62:054503, 2000.

[10] Y. Nambu. Technical report, U. of Chicago Report No. 70-70, 1970.

[11] Nathan Isgur and Jack E. Paton. A Flux Tube Model for Hadrons in QCD. *Phys. Rev.*, D31:2910, 1985.

[12] Claude W. Bernard et al. Exotic mesons in quenched lattice QCD. *Phys. Rev.*, D56:7039–7051, 1997.

[13] Thomas D. Cohen. Quantum number exotic hybrid mesons and large N(c) QCD. *Phys. Lett.*, B427:348–352, 1998.

[14] Eberhard Klempt and Alexander Zaitsev. Glueballs, Hybrids, Multiquarks. Experimental facts versus QCD inspired concepts. *Phys. Rept.*, 454:1–202, 2007.

[15] Andrei Afanasev and Philip R. Page. Photo- and electroproduction of $J^{PC} = 1^{-+}$ exotics. *Phys. Rev.*, D57:6771–6777, 1998.

[16] C. McNeile and C. Michael. Decay width of light quark hybrid meson from the lattice. *Phys. Rev.*, D73:074506, 2006.

[17] W.-M. Yao et al. Review of particle physics. *J. Phys.*, G33:1, 2006.

[18] H. H. Bingham et al. Total and partial γp cross sections at 9.3 GeV. *Phys. Rev.*, D8:1277–1286, 1973.

[19] J. Ballam et al. Vector meson production by polarized photons at 2.8, 4.7 and 9.3 GeV. *Phys. Rev.*, D7:3150–3177, 1973.

[20] Y. Eisenberg et al. Photoproduction of ω mesons from 1.2 to 8.2 GeV. *Phys. Lett.*, B34:439–442, 1971.

[21] Y. Eisenberg et al. Study of high energy photoproduction with positron-annihilation radiation. I. Three-prong events. *Phys. Rev.*, D5:15–38, 1972.

[22] G. Alexander et al. Study of high energy photoproduction with positron-annihilation radiation. II. The reaction $\gamma p \to p\pi^+\pi^+\pi^-\pi^-$. *Phys. Rev.*, D8:1965–1978, 1973.

[23] G. Alexander et al. Study of high energy photoproduction with positron-annihilation radiation. III. The reactions $\gamma p \to p2\pi^+2\pi^-\pi^0$ and $\gamma p \to n3\pi^+2\pi^-$. *Phys. Rev.*, D9:644–648, 1974.

[24] T. Sjöstrand, S. Mrenna, and P. Skands. Pythia 6.4 Physics and Manual. Technical report, Lund University, 2006. hep-ph/0603175 and http://www.thep.lu.se/~torbjorn/Pythia.html.

[25] A. Dzierba. Comparing Pythia Simulations with Photoproduction Data at 9 GeV. Technical report, GlueX Document, 2007. GlueX-doc-856-v1.

[26] J. Ballam et al. Energy dependence of the reaction $\gamma p \to \rho^-\Delta^{++}$. *Phys. Rev.*, 26:995–997, 1971.

[27] N. Kolev et al. Dependence of the spatial and energy resolution of BCAL on segmentation. Technical report, GlueX Document, 2007. GlueX-doc-659-v2.

[28] B. Leverington. Analysis of the BCAL beam tests. Technical report, GlueX Document, 2007. GlueX-doc-804-v4.

[29] R. Lindenbush. A study of the reaction $\pi^- p \to \eta\pi^0 n$ at 18 GeV/c. Ph. D. Thesis - Indiana University, 1998.

[30] A. R. Dzierba et al. A study of the $\eta\pi^0$ spectrum and search for a $J^{PC} = 1^{-+}$ exotic meson. *Phys. Rev.*, D67:094015, 2003.

[31] R. T. Jones. Detector Models for GlueX Monte Carlo Simulation: the CD2 Baseline. Technical report, GlueX Document, 2006. GlueX-doc-732-v4.

[32] D. Lawrence and S. Taylor. GlueX Simulation Geometry Version 4.0. Technical report, GlueX Document, 2007. GlueX-doc-853-v8.

[33] D. Lawrence. Track fitting in GlueX: Development Report III. Technical report, GlueX Document, 2007. GlueX-doc-761-v2.

[34] H. Wirth, *et al.* (The JETSET Collaboration). Particle Identification with the JETSET Straw Chambers. Nucl. Instrum. Methods A**367**, 248, (1995).

[35] M. Bellis. Technical report, GlueX Document, 2008. GlueX-doc-971-v1.

[36] A. R. Dzierba et al. A partial wave analysis of the $\pi^-\pi^-\pi^+$ and $\pi^-\pi^0\pi^0$ systems and the search for a $J^{PC} = 1^{-+}$ meson. *Phys. Rev.*, D73:072001, 2006.

[37] The Hall D Collaboration, (R. Clark *et al.*). A Search for QCD Exotics Using a Beam of Photons. The GlueX Design Report, version 4, November 2002. GlueX-doc-58.

[38] P. Eugenio, J. Kaditz, C.A. Meyer and B. Zaroukian. A Study of leakage in Partial Wave Analysis for the HallD Detector at Jefferson Lab GlueX-doc-51, December 2001.